Numerical investigation of starting turbulent buoyant plumes released in neutral atmosphere

Kiran Bhaganagar[1],[†] and **Sudheer R. Bhimireddy**[1]

[1]Department of Mechanical Engineering, University of Texas, San Antonio, TX 78249, USA

A fundamental study has been conducted to understand the mean and turbulence characteristics and their role in mixing processes of starting turbulent plumes initiated by a heated area source and released into a neutral atmosphere. Large eddy simulation has been performed in a domain of size 7 km (vertical) and 4 km × 4 km (horizontal) for five different cases with surface heat flux varying from 0.5–2.5 km s^{-1}. With increasing buoyancy flux, the plume Reynolds number Re (based on the maximum centreline velocity) increases from 6×10^7–10^8; however, the Froude number Fr does not increase monotonically with increasing B_o, it varies from 1.091–1.149. Key physics that contributes to mixing and entrainment of ambient fluid into the plume has been investigated. The buoyancy- and shear-production of turbulence kinetic energy contributes to the mixing processes within the plume. The characteristic features of a starting plume are: the presence of a spiralling columnar neck region surrounding the central core that extends to $5D$ (D is the source diameter), and which is capped with an unsteady head region that actively entrains fluid due to instabilities at the plume interface. Formation of vortex rings and instability mechanisms are linked to the entrainment process. Unsteady entrainment has been calculated using first principles, and the results revealed that entrainment, though negligible initially, initiates with the growth of the instabilities in the head region of the plume, and it correlates with the local Reynolds number in the head region.

Key words: plumes/thermals, mixing and dispersion, turbulence simulation

1. Introduction

Turbulent plumes are initiated and maintained by pure buoyancy forces, such as a heated source, or due to the release of a lighter buoyant fluid into the ambience. The buoyant plumes released into the neutral atmosphere rise vertically due to the initial buoyancy flux, and the buoyancy flux remains unchanged with height as the ambient fluid carries no heat anomaly. Turbulent plumes form an important class of fluid dynamic problems which are ubiquitous in the environment, and they occur due to both natural and man-made geophysical phenomena. The natural plumes that occur include thermal plumes that arise due to the convective heating on Earth's surface (Morton 1957, 1959; Woods 2010), the overflows on the continental slopes of the oceans at high altitudes (Baines 2001; Özgökmen *et al.* 2003), volcanic eruptions (Ernst *et al.* 1996; Carazzo, Kaminski

† Email address for correspondence: kiran.bhaganagar@utsa.edu

& Tait 2008) and sea ice plumes (Skyllingstad & Denbo 2001; Widell, Fer & Haugan 2006), to name just a few. Man-made plumes include smoke stacks (Briggs 1972), the release of chemicals into the atmosphere (Bhaganagar & Bhimireddy 2017) and wildland fires (Fromm & Servranckx 2003; Kahn *et al.* 2008). Buoyant plumes that occur in the environment have very high Reynolds numbers and as they spread they entrain the ambient fluid into the plume resulting in substantial mixing (Woods 2010). Thus, it is important to understand the unsteady flow dynamics and mixing processes from the initial time (i.e. the release from the source), and flow processes in the near-source region of the starting plumes from an area release will provide key direction for future studies on geophysical plume dynamics.

The experiments of Turner (1962) on starting buoyant plumes revealed that during the initial stages of the formation of the turbulent buoyant plume, a well-defined plume head appears that is unsteady in nature, and a steady plume forms behind the head. Turbulent plumes grow vertically, spreading radially as a result of entraining ambient fluid into the plume at the boundary or the interface between the plume and the ambience, and also due to mixing at the central core (Turner 1969). The classical theoretical plume model in a homogeneous fluid was first pioneered by Morton, Taylor & Turner (1956) for turbulent buoyant convection from a maintained localized source, and it is based on conservation of mass, buoyancy and momentum. However, the entrainment is an unsteady process and it is not clear if assuming a constant entrainment during the plume growth process is justified.

The data in the near-source region of pure plumes (i.e. $z = 0$–$15D$, D being the source diameter) is very limited. The earlier data include the experiments of Shabbir & George (1994), where a buoyant plume was generated by forcing a jet of hot air into an isothermal and quiescent ambience. The flow was not fully turbulent at the source. The measurements further from the source (i.e. beyond $20D$) confirmed the similarity solutions presented by Batchelor (1954) for three-dimensional axisymmetric plumes. The velocity profiles were observed to be 10 % wider than the temperature profiles. Similar validation of the similarity solutions has been reported by Papanicolau & List (1988). However, there is no consensus on the centreline values of the mean velocity and buoyancy profiles, nor the turbulence measurements. The study focuses on area-released starting plumes that are generated from purely buoyant sources, and these are fundamentally different compared with the plumes generated when a jet transitions to the plume regime and eventually reaches steady-state conditions. A few experimental studies by Friedl, Härtel & Fannelop (1999) and Epstein & Burelbach (2001), qualitative observations by Schultz, Delaney & McDuff (1992) and numerical simulations by Pham, Plourde & Doan (2007) and Plourde *et al.* (2008) for an area-release plume, have revealed that the key characteristic of plume release from an area source is the existence of a well-defined converging–diverging region resulting in a necking type of configuration. Within the neck region, the half-width of the plume reaches a minimum value, as the flow accelerates the centreline velocity reaches a maximum value, as shown by Fanneløp, Hirschberg & Küffer (1991), Fanneløp & Webber (2003) and Kaye & Hunt (2009). It is not clear if the flow dynamics in the neck region scales with the source conditions. Further, the transient behaviour in the neck region is still unclear.

Adding to the complexity, more recent experiments have revealed significant discrepancies in plume characteristics among different experiments, for example, the ratio of the mean turbulent fluxes to the mean advective flux was found to be 40 % by Kotsovinos & List (1977), whereas Ramaprian & Chandrasekhara (1989) reported it to be 15 %. Surprisingly, there exist very few studies that analyse buoyant plumes compared with those

of turbulent jets (Van Reeuwijk *et al.* 2016). Devenish, Rooney & Thomson (2010) perform a quantitative comparison of vertical buoyant plumes in a uniform environment generated using large eddy simulation (LES) with plume theory. The statistics were calculated over a long time period after the plume reached steady-state. They demonstrated that at heights 20–35D, the centreline velocity and the reduced gravity exhibit expected scalings of $z^{-1/3}$ and $z^{-5/3}$, respectively, where z is axial direction; and the mean velocity and temperature are fitted by Gaussian profile. The mean state and second-order turbulence statistics of a plume demonstrate a self-similar trend. The trend of the turbulence with respect to the mean statistics is not clear (i.e. what is the ratio of the root mean square (r.m.s.) of the centreline velocity to the mean velocity, or the ratio of the r.m.s. of the temperature fluctuations to the mean temperature or the turbulence transport to advection at different heights). From the analysis of plumes at low Reynolds number, buoyancy enhances mixing and thus the entrainment coefficient of plane and axisymmetric plumes is higher than of jets (Linden *et al.* 2000; Fischer *et al.* 2013). An experimental study of turbulent buoyant plumes released from a source of diameter 1 m by O'hern *et al.* (2005) has revealed that Rayleigh–Taylor instabilities due to the density differences at the base of the plume leads to the vortex that grows to dominate the flow. However, this instability has not been reported by other experimental or numerical studies.

Overall, based on the existing literature, it is clear that most of the work on buoyant plumes has been confined to the study of turbulent jets or transition from jets to buoyant plumes at low Reynolds numbers, which corresponds to idealistic source conditions (i.e. low surface heat flux). There exists very little either experimental or numerical data on buoyancy-dominated plumes at atmospheric convective scales in the region close to the source ($z = 0$–15D), where D is source diameter. The present work is motivated by the need to quantify the entrainment of plumes at environmental scales. Turbulent mixing contributes significantly to the entrainment, as both the shear-generated and buoyancy-generated sources contribute to the turbulent kinetic energy (TKE). A large eddy simulation is conducted to understand the fundamental flow dynamics, turbulent mixing and entrainment processes. The governing equations for the numerical model are the compressible Euler equations, and they are solved using large eddy simulation within the framework of the weather research and forecasting (WRF) model (Skamarock *et al.* 2008). In the present work, we propose addressing the following questions.

(i) What are the scaling laws for the mean fields and turbulence processes? What are the key mechanisms for the generation of turbulence kinetic energy? What are the scales at which the mean field and the turbulence reach a similarity solution of an axisymmetric plume, and does the mean flow reach self-similarity faster than turbulence?

(ii) What is the role of the head of the plume in the mixing and entrainment process for the starting plumes, and what is the dynamic contribution of the neck region in mixing processes?

(iii) How to quantify the highly unsteady entrainment and mixing process, and what is its relation to the large-scale structures and vorticity generation mechanism?

The turbulent buoyant plume is generated from an axisymmetric heated source of diameter D into a quiescent environment. Detailed analysis of the mean flow, turbulent characteristics and flow structures is conducted in the near-source region from $z = 0$–15D.

The manuscript is arranged as follows: § 2.1 describes the LES methodology using WRF framework and § 2.2 describes the details of the case studies presented in this work.

Section 3 describes the flow characteristics of both mean flow and turbulent statistics, followed by the entrainment and mixing characteristics of the plume. The discussion and conclusions are presented in § 4.

2. Methodology

2.1. *Numerical model*

The model equations solved are the compressible Euler conservative equations in flux formulation (Laprise 1992; Garratt 1994; Batchelor 2000; Yang & Cai 2014). Equation (2.1) represents the conservation of mass, (2.2) represents the conservation of momentum and (2.3) represents the conservation of energy in the model domain,

$$\partial_t \rho + \partial_i(\rho u_i) = 0, \tag{2.1}$$

$$\partial_t(\rho u_i) + \partial_j(\rho u_i u_j) + \partial_i p + \delta_{i3}\rho g = \partial_j(\rho K_j \partial_j u_i) + \partial_i(\rho K_j \partial_j u_i), \tag{2.2}$$

$$\partial_t(\rho\theta) + \partial_i(\rho u_i \theta) = \partial_i(\rho K_i^h \partial_i \theta) - \delta_{i3}\rho g H_o, \tag{2.3}$$

where u_i represents the velocities in x, y and z directions, p is the pressure, θ is the potential temperature, ρ is the density, g is acceleration due to gravity and K_i is the horizontal ($i = 1, 2$) and vertical ($i = 3$) eddy viscosity determined based on 1.5-order TKE closure scheme (Deardorff 1980; Moeng 1984; Holt & Raman 1988), i.e. $K_i = C_k l_i \sqrt{e}$. C_k is constant ($= 0.1$), l_i represents the mixing length in horizontal ($i = 1, 2$) and vertical ($i = 3$), and e is subgrid TKE which is predicted by

$$\partial_t(\rho e) + \partial_i(\rho u_i e) = \rho K_i[\partial_i u_j + \partial_j u_i]^2 - \rho K_3 N^2 - \rho \frac{C e^{3/2}}{l}, \tag{2.4}$$

where N is the Brunt–Väisälä frequency calculated as $N^2 = (g/\theta)\partial_z \theta$, $C = 1.9C_k + max[0, 0.93 - 1.9C_k]l/\Delta s$, $\Delta s = \sqrt[3]{\Delta x \Delta y \Delta z}$, $l = min[\Delta s, 0.76\sqrt{e}/N]$ and Δx, Δy, Δz represent the grid resolution in horizontal and vertical. Based on the potential temperature gradient, the horizontal and vertical mixing lengths are estimated. For $N^2 > 0$, $l_{1,2} = l_3 = l$ and for $N^2 \leq 0$, $l_{1,2} = l_3 = \Delta s$. Here, K_i^h in (2.3) represents the horizontal ($i = 1, 2$) and vertical ($i = 3$) eddy diffusivity of heat estimated by multiplying the earlier predicted K_i with $Pr_l = 1 + 2(l_i/\Delta s)$.

The above-mentioned model equations are solved using a finite difference method with staggered positioning of variables (Arakawa & Lamb 1977). This means vertical velocity (w) is estimated on the face centre beginning at the wall, $z = 0$, and ending at top of the domain, $z = L_z$. The horizontal velocities (u and v) and scalars (θ, p and ρ) are computed on a grid that starts at $z = \Delta z/2$ and ends at $z = L_z - \Delta z/2$. The spatial derivatives are estimated using a fifth-order accurate upwind approximation for horizontal, and third-order accurate for vertical terms. The time-split integration based on a regular third-order Runge–Kutta scheme is used to march the model equations forward in time. Wicker & Skamarock (2002) integrated the compressible Navier–Stokes equations using two time-splitting methods, namely third-order Runge–Kutta time scheme and Crowley advection scheme, and found that third-order Runge–Kutta scheme offers best performance for atmospheric models.

The numerical framework used differs from existing studies such as Pham *et al.* (2007), Devenish *et al.* (2010), Taub *et al.* (2015) and Van Reeuwijk *et al.* (2016) as the present formulation uses a fully compressible set of governing equations with the variables cast in their flux form, which makes it applicable to flows occurring at atmospheric scales with realistic background conditions.
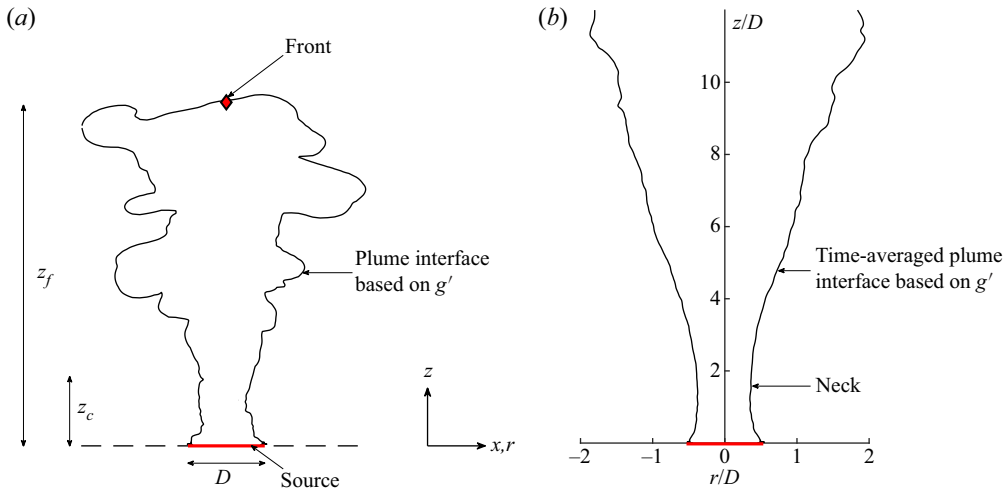
FIGURE 1. Buoyant plume schematics in the study. (*a*) Instantaneous plume interface and leading edge location defined based on the reduced gravity threshold criterion, z_f and z_c shown in panel (*a*) represent the instantaneous front height and axial location of maximum centreline velocity. (*b*) Time-averaged plume interface showing the neck region close to the source.

2.2. *Case set-up*

The schematic of the physical problem that is being investigated in this study is given in figure 1(*a*). At initial time $t = 0$, the ambient fluid of density ρ_0 and temperature θ_0 is at rest. A circular region of the source at the bottom boundary with diameter $D(= 400$ m$)$ is heated with a constant surface heat flux (H_o). The heating causes a temperature difference (or density difference $\Delta\rho$ with respect to the ambient density ρ_0) between the ambient fluid and the source region, which is represented by the reduced gravity $g' = g(\Delta\rho/\rho_0)$. The domain is of size $10D \times 10D \times 17.5D$ along the two cross-stream (horizontal) and axial (vertical) directions, where D is the diameter of the source located at the centre of the bottom boundary. The computational domain is discretized using a Cartesian grid with $100 \times 100 \times 700$ equidistantly spaced nodes in the cross-stream (horizontal) and axial (vertical) directions. The time step used in the simulations is chosen to be $1/6$ s in order to limit the Courant–Friedrichs–Lewy number to 0.2. Periodic boundary conditions were imposed on the side boundaries, while a constant pressure boundary condition was imposed on the top. At the centre of the bottom boundary, where the source is located, a constant surface heat flux is specified while the remaining bottom boundary has zero heat flux across. Table 1 summarizes the initial conditions considered for the simulation. A 5 % perturbation is imposed on the temperature field close to the source location by the cell perturbation method (Buckingham *et al.* 2017). By imposing the perturbations on the temperature field, the turbulence build-up is supported by local buoyancy variations rather than the velocity field, as has been the case in many other studies (Schlüter, Pitsch & Moin 2004; Wu 2017).

The simulations have been performed for five different cases with source g' of 0.082, 0.145, 0.185, 0.237 and 0.272, respectively. Details of the simulations are given in table 1. The source heat flux is maintained at a constant value of H_o which corresponds to 0.5, 1.0, 1.5, 2.0 and 2.5 km s^{-1}, respectively, for cases 1–5, which resulted in a $\Delta\theta_0 = \theta_0 - \theta_a \approx 2$, 4.5, 5, 7.3 and 8.4 K (θ_a is the ambient temperature inside the domain). The simulation time is made dimensionless using a time scale, $t_0 = D/w_b$, where w_b is the

Variable	Case 1	Case 2	Case 3	Case 4	Case 5
H_o (km s^{-1})	0.5	1.0	1.5	2.0	2.5
$\Delta\theta_0$ (K)	2.55	4.51	5.44	7.36	8.46
g'_0 (m s^{-2})	0.082	0.145	0.185	0.237	0.272
B_o (m^4 s^{-3})	2×10^3	4×10^3	6×10^3	8×10^3	10×10^3
A_1	-82.07	-91.75	-91.39	-88.19	-94.88
A_2	-75.02	-78.34	-81.28	-82.86	-85.39
b_w	0.1103	0.1044	0.1046	0.1065	0.1027
$b_{g'}$	0.1155	0.1129	0.1109	0.1099	0.1082
Fr_{w_c}	1.091	1.089	1.110	1.141	1.149
Re_{w_c}	6.02×10^7	9.12×10^7	1.15×10^8	1.33×10^8	1.47×10^8
$\overline{w_{cmax}}$ (m s^{-1})	6.25	8.30	9.55	11.11	11.99
$\tilde{z}$	1.62	1.63	1.63	1.75	1.75
$\tilde{l}$	0.31	0.32	0.35	0.37	0.37
Re_t	7364	8018	8346	9418	9600

TABLE 1. Initial conditions and dimensionless numbers for cases simulated: H_o is the heat flux supplied at the source; $\Delta\theta_0$ is the initial temperature difference between the source and ambience; g'_0 is the initial reduced gravity at the source; B_o is the rate of buoyancy addition at the source; A_1, A_2 are the Gaussian similarity constants for mean velocity and temperature radial profiles; b_w and $b_{g'}$ are the velocity- and buoyancy-half-widths of the plume scaled by the diameter D; $\overline{w_{cmax}}$ is the time-averaged maximum velocity along the centreline; $\tilde{z}$ and $\tilde{l}$ are the scaled axial location and plume half-width at the maximum velocity position (scaled by D).

buoyant velocity estimated as $\sqrt{g'_0 D}$. All the statistics reported in this study are time averaged starting from the time of formation of a well-defined head (discussed later) until $t/t_0 = 50$. The schematic of instantaneous state of the plume is shown in figure 1(*a*). The time-averaged mean state of the plume is shown in figure 1(*b*). The plume interface is defined based on the g' criterion, i.e. a 1 % threshold value of the source g'.

The plume Reynolds number for the cases studied is defined based on the maximum mean velocity at the centreline ($\overline{w_{cmax}}$) and plume half-width ($\tilde{l}$) at the axial location ($\tilde{z}$) of maximum velocity,

$$Re_{w_c} = \frac{\overline{w_{cmax}}\tilde{l}D}{\nu}, \tag{2.5}$$

where ν is the viscosity of air estimated based on the temperature at $\tilde{z}$. Similarly, the Froude number is defined as a ratio of $\overline{w_{cmax}}$ and buoyancy velocity, w_b,

$$Fr_{w_c} = \frac{\overline{w_{cmax}}}{w_b}. \tag{2.6}$$

The turbulence Reynolds number based on $\overline{w_{cmax}}$, $\tilde{l}$ and subgrid turbulent kinetic energy ($\overline{e}$) is estimated as

$$Re_t = \frac{\overline{w_{cmax}}\tilde{l}D}{\sqrt{\overline{e}}}, \tag{2.7}$$

where Re_t for the cases studied varied from 7364 to 9600 for cases 1–5, respectively.

3. Results

The coordinate system used is as follows: the components of the velocity are the axial velocity (w) along the axial direction (z); the horizontal velocity components are (u) and (v). The leading edge of the plume is defined as the front, and it is mathematically represented as the leading point on the centreline ($r/D = 0$) in the axial direction, where the plume buoyancy (g') is 1 % of source buoyancy (g'_0). Similarly, the plume interface is defined using the g' threshold criterion. The time-averaged plume interface is used to obtain the plume half-width of the buoyancy profile ($b_{g'}$) and of the velocity profile (b_w) at each height. We will refer to these as buoyancy half-width and velocity half-width, respectively. The plume front is defined as the leading location on the centreline of the plume at a given time. The plume velocity (w_f) is defined as the velocity of the plume front.

3.1. *Plume characteristics*

The plume characteristics are discussed first. The analysis of the plume characteristics has been performed for cases 1–5. Figure 2(*a*–*c*) are the plume characteristics for case 2. All the five cases are shown in figure 2(*d*). Figure 2(*a*) shows the velocity and buoyancy half-widths of plumes for case 2. Also shown in the figure are the experimental measurements from Ezzamel, Salizzoni & Hunt (2015). It should be noted that the experimental results are for low buoyancy forcings (with g' of 0.025) compared with the present study. Near the source, the plume radius decreases, reaches a minimum value and then increases, clearly showing a change of curvature from a converging to diverging trend, which is referred to as a neck region and this is a characteristic feature of area-release plumes. We estimated the plume Richardson number Γ (Morton 1959; Hunt & Kaye 2001) using the local volume ($Q(z) = 2\pi \int_0^\infty w(r, z)r\,dr$), momentum ($M(z) = 2\pi \int_0^\infty w^2(r, z)r\,dr$) and buoyancy fluxes ($B(z) = 2\pi \int_0^\infty w(r, z)g'(r, z)r\,dr$),

$$\Gamma(z) = \frac{5}{2^{7/2}\pi^{1/2}\alpha_{ref}} \frac{Q(z)^2 B(z)}{M(z)^{5/2}}, \tag{3.1}$$

where α_{ref} represents the reference entrainment coefficient which is considered to be 0.1 (Morton 1959).

Figure 2(*c*) shows the variation of the plume height and buoyancy half-width in the $t - z$ plane (t is the time and z is the vertical coordinate). Right after the release time, the plume radius decreases (converging trend) and reaches a minimum width beyond which it grows. A dotted line is shown to indicate this neck region. The rate at which the plume height increases is proportional to $t^{3/4}$, as depicted by the solid line which represents the 3/4 power law. The presence of the neck has been confirmed by experiments, including those by Epstein & Burelbach (2001) and Kaye & Hunt (2009). Finally, the ratio of the buoyancy half-width to the velocity half-width ($\lambda = b_{g'}/b_w$), a measure of the ratio of the spread of the buoyancy to the spread of velocity profiles, is shown in figure 2(*d*). All the five cases have been reported here. The average value of λ above the necking region is found to be around 1.15 for all the cases. For a plume-like behaviour, this value has been reported to be 1.19 (Papanicolau & List 1988), 1.2 (Panchapakesan & Lumley 1993) and 1.0 (Wang & Law 2002). They also noticed a general trend of a decreasing λ with an increasing Richardson number. The Prandtl number ($\langle Pr_T \rangle$), estimated as $\langle Pr_T \rangle = \lambda^{-2}$, has a value of 0.75 ± 0.04. Kaminski, Tait & Carazzo (2005) reported a tendency of Pr to decrease with height. A similar trend is observed in our case. The variation of Γ with height for case
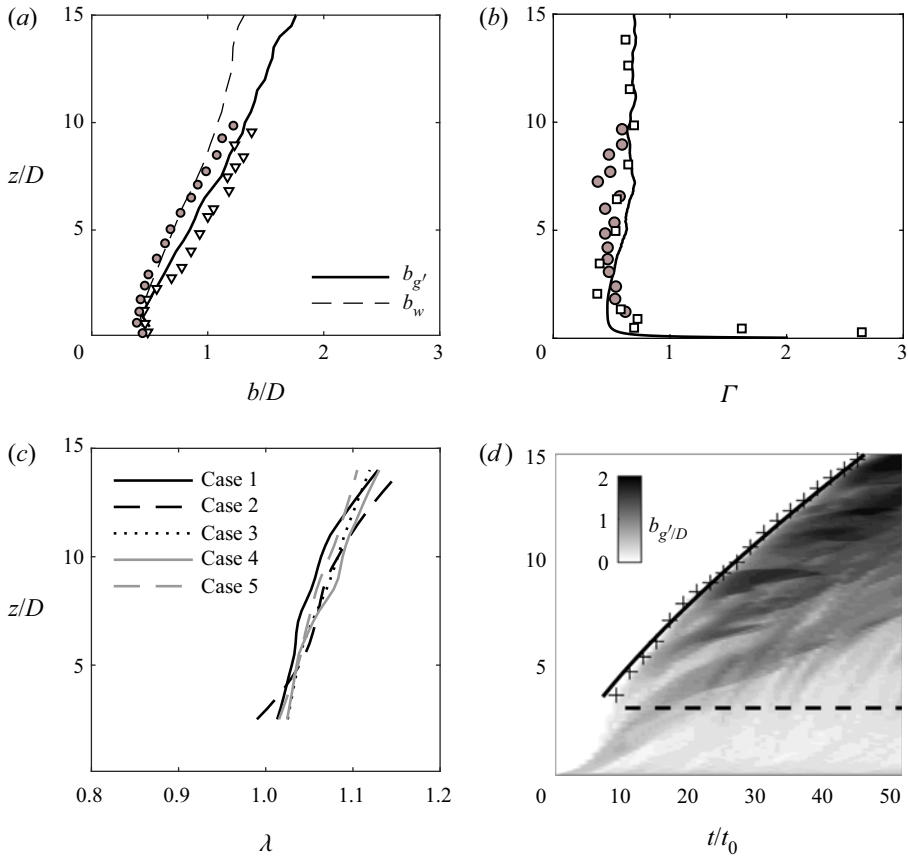
FIGURE 2. (*a*) Variation of velocity- and buoyancy-half-widths of the plume with height for case 2. (*b*) Variation of plume Richardson number with height for case 2. (*c*) For case 2, time–height variation of buoyancy half-width. The $(+)$ symbols represent the plume front and the solid line is 3/4 power law with respect to the time, and the dashed line represents the mean neck location along the plume axis. (*d*) For all the five cases, axial profile of $\lambda = b_{g'}/b_w$. The filled circles and hollow triangles in panel (*a*) represent the half-widths based on buoyancy and velocity from experimental data of Ezzamel *et al.* (2015). Filled circles and squares in panel (*b*) represent the experimental data of Ezzamel *et al.* (2015) and LES data from Devenish *et al.* (2010).

2 is shown in figure 2(*b*). As expected, Γ tends to infinity at the source as this is a pure buoyancy source with no momentum. Here Γ reduces quickly until $\sim 2D$ and thereafter it asymptotes to a value $\Gamma = 1$ after $\sim 5D$, as predicted by the theory for plumes where source $\Gamma \gg 1$ (Hunt & Kaye 2005). The axial profiles of Γ compare well both with the experimental data of Ezzamel *et al.* (2015) and the LES data of Devenish *et al.* (2010).

To quantify the plume's frontal motion, we identify the leading edge, or the plume front (z_f) and plot versus time for cases 1–5 in figure 3(*a*). The front is defined as the farthest point along the centreline of the plume, where the plume interface is based on the threshold criterion of g'. In this plot, the time is normalized by the time scale (t_o) based on the source diameter and buoyancy velocity $(w_b = \sqrt{g'_0 D})$. Scaled in this manner, after the formation of the well-defined head (this will be discussed later on), the front (z_f) advances at a rate

of $t^{3/4}$. The frontal velocity (w_f) which depends only on the buoyancy flux (B_o) and z_f can be expressed as follows: $w_f = \xi_f B_o^{1/3} z_f^{-1/3}$, where ξ_f is the non-dimensional front velocity. Using the definition $w_f = dz_f/dt$, ξ_f can be mathematically represented as

$$\xi_f = \frac{z_f^{4/3}}{B_o^{1/3}(t + t_s)(4/3)}, \tag{3.2}$$

where t_s is the time take for the head to form. The variation of non-dimensional velocity ξ_f is plotted in figure 3(b). The plumes travel with a front velocity given as $w_f \approx 2.0 B_o^{1/3} z^{-1/3}$. The asymptotic value of non-dimensional front velocity scale (ξ_f) reached for all the cases is in the range of 1.89–2.05, matching closely with the 1.99 observed in Bhamidipati & Woods (2017). The Froude number for the cases has been calculated using the maximum centreline mean velocity and the buoyancy velocity. They are found to be 1.091, 1.089, 1.110, 1.141 and 1.149 for cases 1–5, respectively.

Similar to the argument we made for the front velocity, the maximum centreline mean velocity can be scaled in terms of B_o and the height (z_c) where the maximum velocity occurs, and can be expressed as $w_c = \xi_{wc} B_o^{1/3} z_c^{-1/3}$, where ξ_{wc} is the non-dimensional velocity, and the integration will lead to an expression for $\xi_{wc} = z_c^{4/3}/B_o^{1/3}(t + t_s)(4/3)$. The variation of ξ_{wc} is plotted in figure 3(c). The non-dimensional maximum centreline mean velocity has a mean value of 2.83 with a standard deviation of 0.2. It should be noted the scatter is observed in ξ_{wc} as this is the variation of the instantaneous axial location of the maximum centreline velocity, whereas the mean component is used to determine the decay rate. It can be established that for a pure plume in a neutral environment, the ratio of the non-dimensional front velocity to maximum centreline mean velocity is 0.7 for all the five cases. It is clear that as the plume develops, the fluid in the trailing region of the flow (as the maximum centreline mean velocity occur close to the source, which is in the range of $1.5D$–$1.8D$ for the five cases) travels faster than the frontal region and thus trailing source fluid is continuously fed into the frontal region or the head of the plume causing unsteady effects. This is a characteristic feature of the starting plumes that results in the dilution and mixing of the head region of the plume that is constantly fed by the trailing edge of the plume. Similar dynamics of source fluid feeding into the active head region from the passive trailing region were also observed in buoyancy driven lock-exchange density currents (Bhaganagar 2017). The maximum centreline buoyancy and maximum centreline velocity are the characteristic buoyancy and velocity scales, respectively. The results have been shown for case 2, and similar values for the non-dimensional front velocity and maximum centreline velocity have been obtained for all the five cases. Turner (1962) found out from his experiments that the front of a starting plume travels with $\approx 61\%$ of the plume velocity at respective heights once it reaches steady-state. In the present study, the plume velocity within the similarity regime is calculated and the ratio came out to be 0.64 ± 0.03, matching closely with the results of Turner (1962) and Bhamidipati & Woods (2017).

3.2. *Mean flow characteristics*

The time-averaged mean flow characteristics at the centreline ($r = 0$) are discussed first. The results for case 2 are shown. Figure 4(a) shows the mean velocity at the centreline normalized by the maximum value ($\overline{w_c}$), plotted against the axial distance from the source z scaled by the source diameter, D. Initially, the centreline mean velocity accelerates up to $z = 1.6D$, reaches a maximum value $\overline{w_{cmax}}$, and starts to decay at a rate of $-1/3$ power
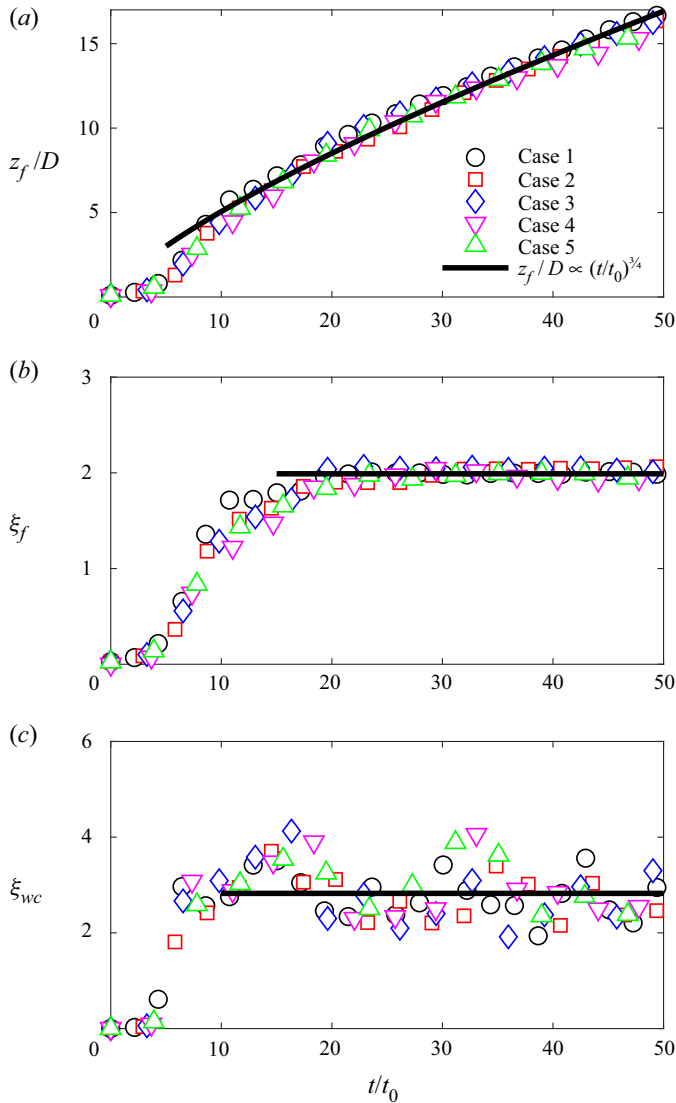
FIGURE 3. Variation in time of (*a*) non-dimensional plume front location (z_f/D), (*b*) non-dimensional front velocity (ξ_f) and (*c*) non-dimensional centreline maximum velocity (ξ_{wc}) with respect to the non-dimensional time (t/t_0). The slope of the decay estimated from the mean centreline velocity is -0.39 ± 0.024 for $2 \leq z/D \leq 12$.

law with height. Also plotted in this figure are the experimental measurements obtained by Pham, Plourde & Doan (2005), LES results of Pham *et al.* (2007) and from the direct numerical simulation (DNS) by Plourde *et al.* (2008). It should be noted that these LES, DNS and experiments have been conducted at much smaller Reynolds number and B_o. The current simulations show a good agreement with previous results. Similar trends have been observed for the other cases; however, the location where is regime shifts to the power-law shows a very weak trend with B_o. For cases 1–5, the location of maximum velocity occurs at $1.62D$, $1.63D$, $1.63D$, $1.75D$ and $1.75D$, respectively.
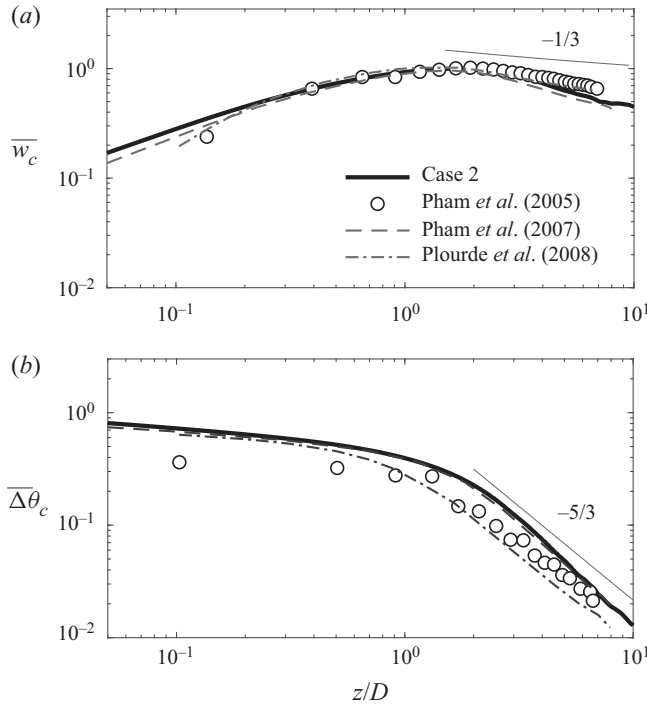
FIGURE 4. For case 2, axial profiles of (*a*) normalized centreline mean velocity and (*b*) normalized centreline mean temperature difference.

Similar analysis has been performed on the mean temperature difference at the centreline ($\overline{\Delta\theta_c}$ in figure 4(*b*)), which is the difference between the temperature in the plume with respect to the ambient temperature. Initially, the centreline mean temperature difference decreases slowly from the source conditions; there is a regime shift and it exhibits a faster decay at a rate of $-5/3$ consistent with theory. An analytical solution for the asymmetric vertical turbulent plume was developed by Batchelor ([1954](#)) who proposed a similarity solution for the mean axial velocity and mean buoyancy acceleration (measure of the temperature difference between the plume and the ambience) as follows: $w = B_o^{1/3} z^{-1/3} f_w(r/z)$ and $g' = B_o^{2/3} z^{-5/3} f_b(r/z)$, respectively, where B_o is the rate at which buoyancy is added at the source, z is the height, r is the radial distance, g' is the buoyancy acceleration, f_w and f_b are the similarity functions. The LES conducted in this study show a good agreement with the theoretical prediction of $-1/3$ and $-5/3$ power law for the centreline mean temperature difference and centreline mean velocity of the axisymmetric plume, respectively.

The radial profiles of the mean flow are discussed next. The radial profiles of the scaled mean axial velocity and the scaled mean temperature difference are plotted at different heights for case 2 in figure 5(*a,b*), respectively. The radial profiles of mean axial velocity and mean temperature exhibit self-preservation characteristics as they collapse to a single curve. The least square Gaussian fit of the mean axial velocity is obtained as $f_w(r/z) = \overline{w_c} \exp[-91.75(r/z)^2]$ for case 2. The coefficient varies with B_o, and the values for cases 1–5 are -82.07, -91.75, -91.39, -88.19, -94.88, respectively. For the mean temperature, this fit is obtained as $f_b(r/z) = \overline{\theta_c} \exp[-78.337(r/z)^2]$. The coefficients
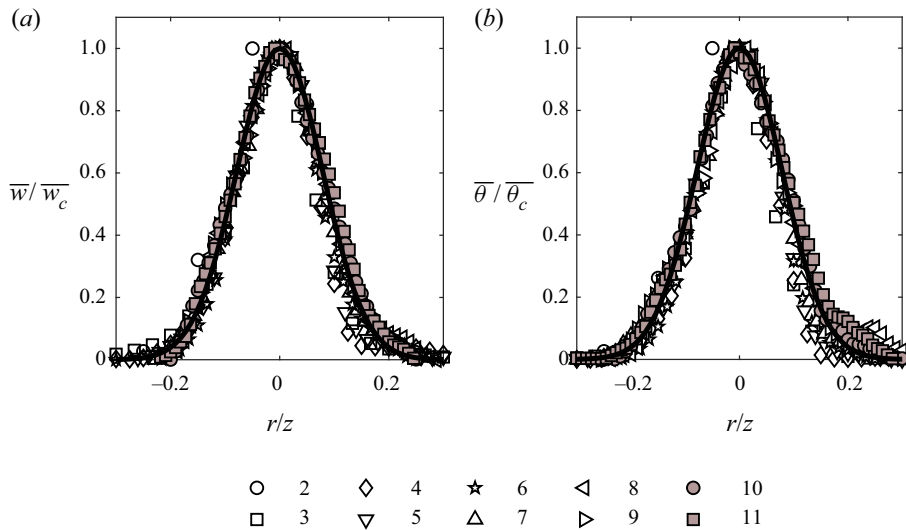
FIGURE 5. Similarity profiles of (*a*) mean axial velocity and (*b*) mean temperature normalized with their respective centreline values for case 2 plotted at different heights above the source. The least squares Gaussian fit is shown by a solid line. Same similarity observed for all the other cases as well.

of the Gaussian fit are close to the ones found by Papanicolau & List (1988) and they depend on B_o as seen in table 1. The coefficients for cases 1–5 are -75.02, -78.34, -81.28, -82.86 and -85.39, respectively. The maximum mean velocity occurs at the centreline ($r = 0$). The buoyancy profiles are wider compared with the velocity profiles, and this is consistent with measurements of plume half-width (b_w) obtained from the mean velocity profile and plume half-width ($b_{g'}$) obtained from the mean buoyancy profile (see figure 2*a*), thus indicating that buoyancy mixing is more dominant than shear mixing in plumes. We will discuss the turbulence characteristics, in detail, in the next section.

The axial evolution of the plume is discussed next. Figure 6(*a*) shows the axial profiles of the mean velocity at different radial locations for case 2. At the centreline $r = 0$, $\overline{w}$ increases slowly from zero to a maximum velocity which occurs at $z = 1.62D$ above the source. Beyond this height, it decays. As seen from figure 4(*a*), the decay has been calculated to be a power law of $-1/3$ with height. At radial distances away from the centreline, the trend of the mean flow is different. For example, at $r = 0.2D$, the mean flow accelerates up to a height of $z = 4D$ and it stays nearly constant above this height. A similar trend is evident at radial distances towards the edge of the plume, the mean flow initially accelerates, and then reaches a quasi-steady value. Figure 6(*b*) shows the profiles of the mean buoyancy at different radial locations.

In conclusion, the mean characteristics of the starting plume reveal that mean flow velocity scales with B_o and z, with the front moving 0.7 times slower than the trailing regime of the plume. The average buoyancy half-width is 10 % wider than the velocity half-width. In the neck region, the mean flow accelerated and reached a maximum velocity, beyond which a regime shift occurs. Mean profiles exhibit self-similarity only above the neck region.
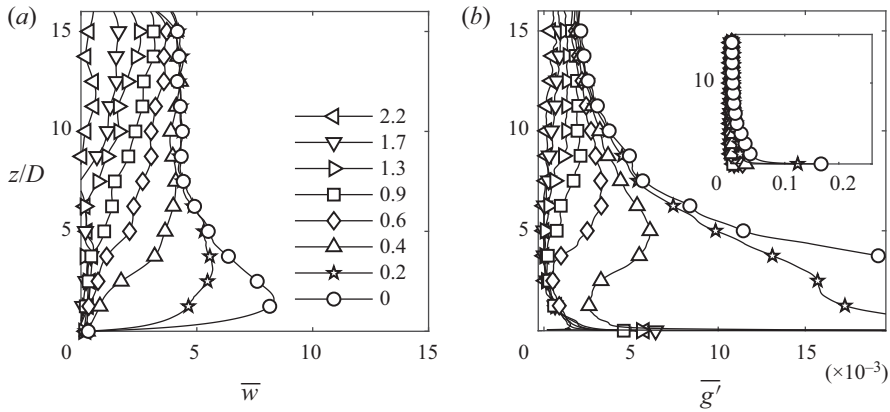
FIGURE 6. Axial profiles of (*a*) mean axial velocity and (*b*) mean buoyancy at radial distances as specified in the legend for case 2.

3.3. *Turbulence characteristics*

We begin the analysis of turbulence by examining turbulence intensity, which is the relative measure of the r.m.s. of velocity and buoyancy fluctuations. All the five cases are analysed here. Figure 7(*a*) shows the scaled axial profiles of the r.m.s. of buoyancy fluctuations at the centreline, while figure 7(*b,c*) show the scaled axial profiles of the r.m.s of the axial velocity and horizontal velocity fluctuations at the centreline, respectively. In the near-source region the buoyancy and velocity fluctuations develop and reach a quasi-equilibrium state away from the source. The θ_{rms} varies between 0.48–0.53 fraction of the mean temperature for different cases. For a fully developed plume, this value has been reported to be in the range of 0.36–0.46 (George, Alpert & Tamanini 1977; Ezzamel *et al.* 2015; Van Reeuwijk *et al.* 2016) as shown in table 2. The fractional values of w_{rms} and u_{rms} with respect to the mean centreline velocity vary from 0.31–0.35 and 0.21–0.24, respectively. These values have been reported to be in the range of 0.19–0.30 and 0.15–0.20, respectively (see table 2). Figure 7(*d*) shows the correlation between axial velocity fluctuation and buoyancy fluctuation, $\overline{w'\theta'}$, which achieves a maximum value at a height of $z = 2D$–$4D$, and corresponds to the 0.11–0.13 fraction of the correlation of mean axial velocity and buoyancy. As reported in previous experiments for steady-state plumes, the relative buoyancy fluctuations in starting plumes are stronger compared with the velocity fluctuations. This is reasonable to expect, as plumes are buoyancy driven in nature.

The radially averaged profiles of the r.m.s. of the axial and radial velocity fluctuations and buoyancy fluctuations for all the five cases are shown in figure 8. The peak r.m.s of velocity and buoyancy fluctuations increases with increasing source buoyancy B_o. The peak value of axial velocity fluctuations occurs at a height of $z = 4D$ above the source, whereas the radial velocity fluctuations reach a maximum at $5D$. At the centreline, due to the presence of the source, the buoyancy fluctuations are highest at the surface. They initially decay up to height to $z = 1D$, beyond which they reach a quasi-equilibrium value in the region $z = 1D$–$4D$, followed by monotonic decay. The radially averaged buoyancy profile exhibits a similar trend. For higher source strength, B_o, turbulence velocity fluctuations persist even at heights corresponding to $z = 15D$; on the other hand, the buoyancy fluctuations decay much faster as they vanish around $z = 10D$ above the source for all the cases. The decay of the radial velocity fluctuations with height is much
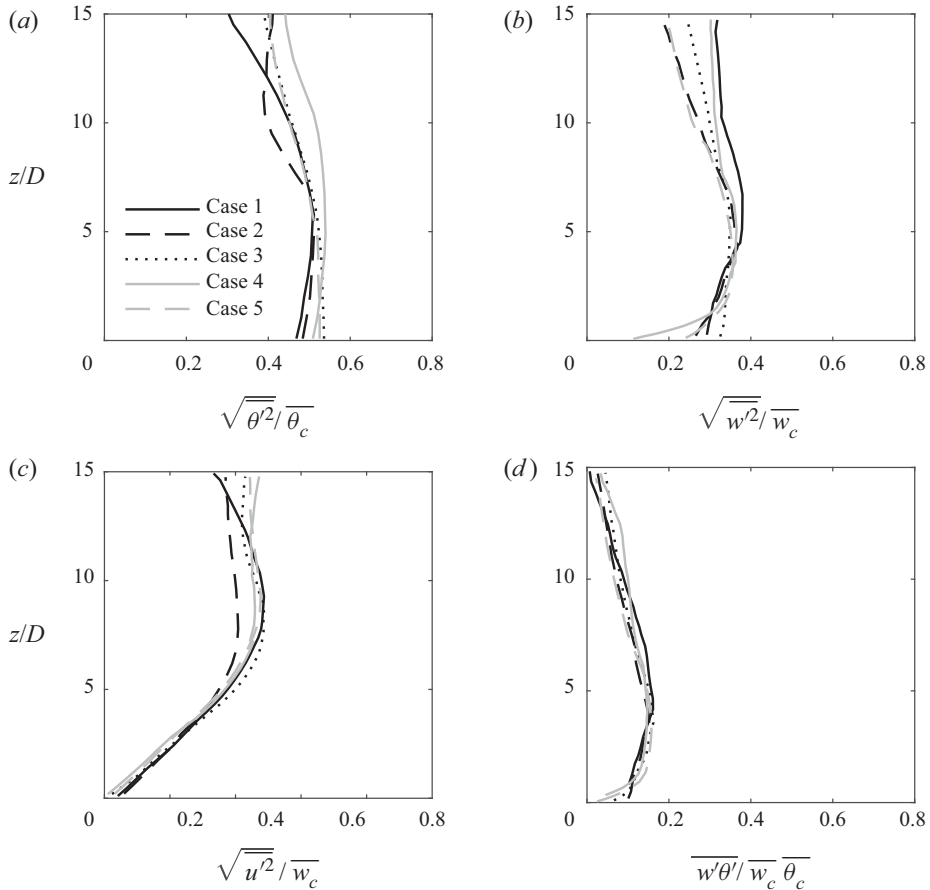
FIGURE 7. Axial variation of (*a*) r.m.s. of temperature fluctuations scaled by centreline mean temperature, (*b*) r.m.s. of axial velocity fluctuations scaled by centreline mean axial velocity, (*c*) r.m.s. of horizontal velocity fluctuations scaled by centreline mean axial velocity, (*d*) r.m.s. of turbulent buoyancy flux normalized with correlation of centreline mean velocity and centreline mean temperature.

slower compared with that of the axial velocity fluctuations. The peak turbulence intensity occurs higher above the source compared with the peak centreline mean velocity, which occurs around $z = 1.2D$. The location of the peak r.m.s. velocity fluctuations coincide with the beginning of the instabilities leading to mixing and entrainment. This will be discussed further in the next section. The axial profiles of TKE are shown in figure 8(*d*). Turbulence kinetic energy reaches a maximum value at $4D$, and the higher the B_o, the higher is the TKE magnitude. Turbulence kinetic energy decays with height, but is still persistent at $z = 15D$.

Turbulence kinetic energy profiles at different radial locations for case 2 are plotted in figure 9(*a*). At the centreline ($r/D = 0$), the maximum TKE occurs at $z = 4D$ from the source. Off the centreline, the location of the maximum TKE moves away from the source with increasing radial distance from the centreline. To estimate at what radial distances the maximum TKE occurs at different height above the ground, figure 9(*b*) shows the

	$w_{rms}/\overline{w_c}$	$u_{rms}/\overline{u_c}$	$\theta_{rms}/\overline{\theta_c}$	$\overline{w'\theta'}/\overline{w_c}\overline{\theta_c}$	$\overline{w'\theta'}/w_{rms}\theta_{rms}$
Case 1 ($g' = 0.082$)	0.35	0.23	0.49	0.13	0.68
Case 2 ($g' = 0.145$)	0.32	0.21	0.46	0.11	0.69
Case 3 ($g' = 0.185$)	0.33	0.23	0.50	0.12	0.69
Case 4 ($g' = 0.237$)	0.34	0.24	0.53	0.13	0.71
Case 5 ($g' = 0.272$)	0.31	0.22	0.48	0.11	0.69
George *et al.* (1977)	0.25	—	0.38	0.07	0.67
Pham *et al.* (2005)	0.23	0.19	—	—	—
Van Reeuwijk *et al.* (2016)	0.19	0.15	0.56	0.18	—
Pham *et al.* (2007)	0.25	—	0.36	0.07	0.62
Plourde *et al.* (2008)	0.22	0.18	0.35	—	—
Wang & Law (2002)	0.26	0.19	0.42	0.06	—
Ezzamel *et al.* (2015)	0.30	0.20	—	—	—
Papanicolau & List (1988)	0.25	0.17	0.22	0.04	—
Marjanovic, Taub & Balachandar (2019)	0.25	0.17	0.22	0.04	—
Taub *et al.* (2015)	0.25	0.21	0.48	0.07	—

TABLE 2. Comparison of the r.m.s. of turbulence fluctuations against the existing literature. First five rows correspond to present study cases 1–5.

radial location corresponding to the maximum TKE at each height. In the near-source region, the maximum TKE occurs at the centreline. However, at spatial locations beyond the height of $5D$, the location of the maximum TKE moves radially away towards the plume interface. The maximum TKE at each height is also plotted here. Far away from the source at $z = 15D$, the TKE is still strong and it has a magnitude which is 33 % of the maximum TKE. Figure 9(*c*) shows the TKE scaled by maximum TKE in the plume (this occurs at the centreline) plotted against radial distance scaled by the height. As all the profiles have been scaled by a common denominator, the relative strengths of the TKE at different elevations is apparent. Scaled in this manner, the TKE profiles show a similarity radially away from the centreline. Difference in TKE is evident up to $r = 0.1z$, and beyond which the profiles collapse in both near- and far-regions from the source.

The scaled radial profiles of the r.m.s. of the velocity and buoyancy fluctuations for case 2 are plotted in figures 10(*a*) and 10(*b*), respectively. The mean flow has reached a similarity at these time scales, whereas the turbulence has not yet reached a state of self-similarity. There is a significant scatter present for the similarity profiles. The radial profiles of the shear driven and the buoyancy driven TKE production for case 2 are shown in figures 11(*a*) and 11(*b*), respectively. The TKE production is due to combination of shear production ($P_s = -\overline{u'w'}[\partial\overline{w}/\partial r + \partial\overline{u}/\partial z]$) and buoyancy production ($P_b = -\overline{w'\theta'}(g/\overline{\theta})$) of turbulence. The Reynolds stresses (i.e. $\overline{w'u'}$) contribute to the shear production, and temperature velocity correlation ($\overline{\theta'w'}$) contribute to the buoyancy production of TKE. As seen in figure 11(*a*), peak P_s occurs at an off-axis location of $0.25D$ from the axis at $z = 2D$–$4D$. At these heights, the peak P_b also occurs at the same radial location. In the near-source region, both shear and buoyancy production are maximum at $r = 0.25D$, whereas the maximum TKE occurs at the centreline, clearly indicating a radial transport of turbulence towards the axis. Away from the source, at heights $z = 4.5D$–$6.5D$, the peak P_s is off-axis at $r = 0.4D$. This is mainly due to the fact that in the near-source region, the shear production is mainly dominant due to the shearing mechanism at the centreline. On
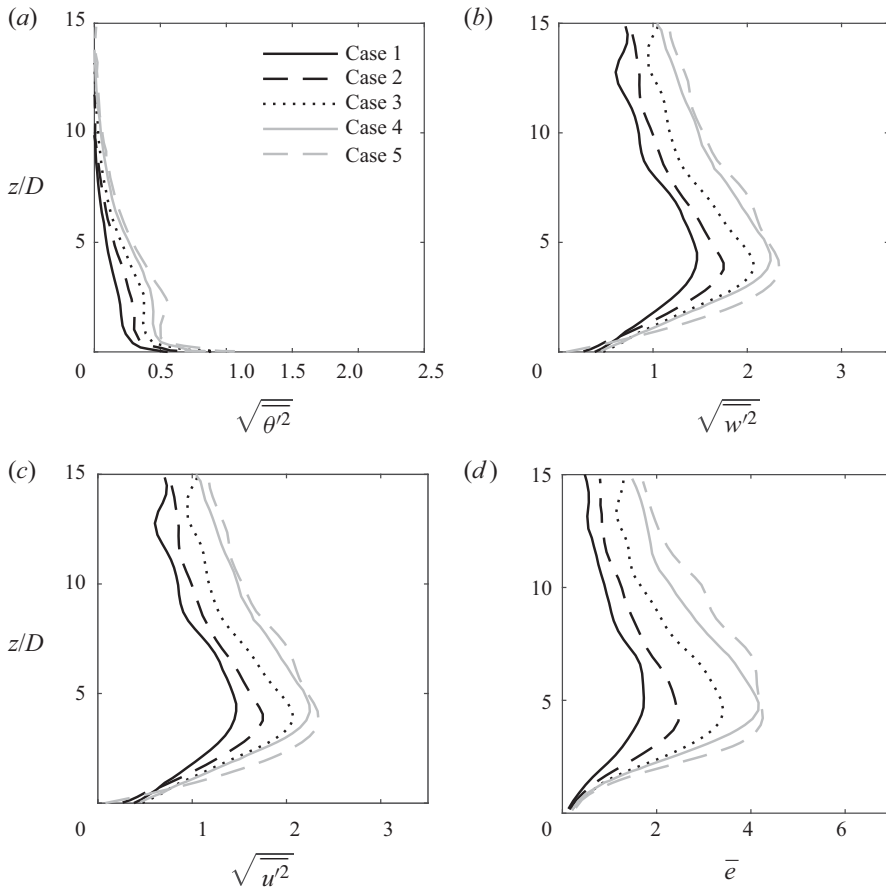
FIGURE 8. Axial variation of radially averaged profiles of the r.m.s. of the (*a*) temperature fluctuations, (*b*) axial velocity fluctuations, (*c*) horizontal velocity fluctuations, (*d*) turbulent kinetic energy for all the cases.

the other hand, the peak P_b is confined to $r = 0.2D$–$0.4D$. The magnitude of the buoyancy production is higher compared with the shear production of turbulence, as expected. The driving force is due to buoyancy flux and only a portion of the buoyancy flux is converted to the momentum flux.

In summary, the starting plumes from an area release are characterized by a converging–diverging neck that corresponds to a location of minimum radius and maximum velocity. The axial mean velocity develops a similarity solution of the form $\overline{w_c} = B_o^{1/3} z^{-1/3} e^{A_1 (r/z)^2}$ and the axial buoyancy has a form $\overline{\theta_c} = B_o^{2/3} z^{-5/3} e A_2 (r/z)^2$, where $\overline{w_c}$ and $\overline{\theta_c}$ denote the mean centreline velocity and temperature, respectively, and A_1 and A_2 correspond to the Gaussian similarity coefficients for $\overline{w_c}$ and $\overline{\theta_c}$ given in table 1. It is estimated from λ that the neck exists and extends to $5D$. Turbulent kinetic energy is generated due to a combination of shear and buoyancy driven production mechanisms. Both the peak TKE production mechanisms, P_s and P_b, occur in the neck region, off-axis from the centreline at heights of $z = 3D$ and $z = 2D$, respectively. The peak TKE production occurs off-axis but due to radial transport mechanisms the peak TKE occurs
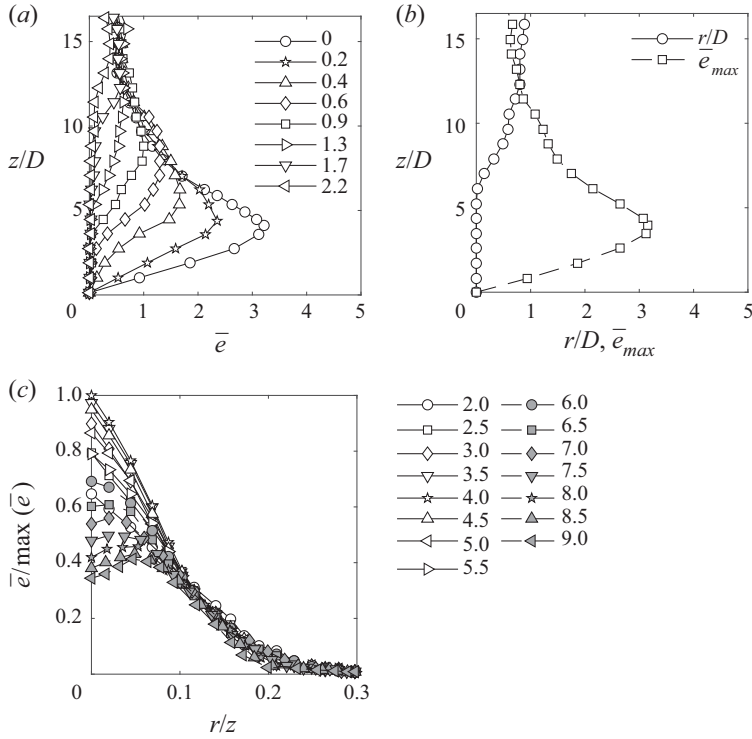
FIGURE 9. For case 2, (*a*) axial profiles of TKE at various radial distances, (*b*) radial location of the maximum TKE (circle symbols) and the magnitude of the maximum TKE at each axial plane, (*c*) radial profiles of TKE normalized with the maximum value at different axial distances given in the legend below.
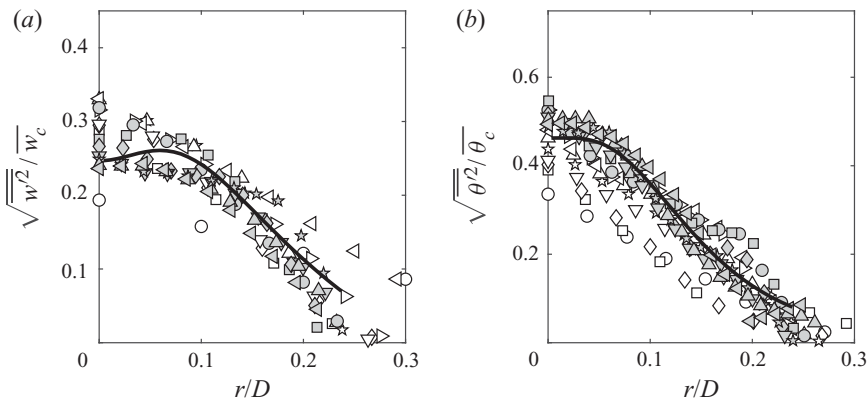

FIGURE 10. Radial profiles of the scaled (*a*) r.m.s. of the axial velocity fluctuations, (*b*) r.m.s. of the buoyancy fluctuations for case 2. The symbols correspond to the locations as given in figure 9(*c*).
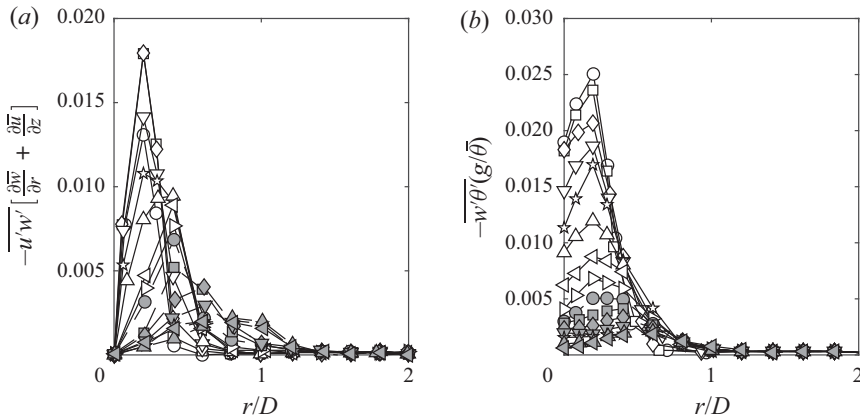
FIGURE 11. Radial profiles of (*a*) TKE shear production (P_s) and (*b*) TKE buoyant production (P_b) at various axial locations along the plume growth for case 2. The symbols correspond to the locations as given in figure 9(*c*).

at the centreline. The maximum TKE occurs at a height $4D$ above the source and beyond which it starts to decay. The buoyancy fluctuations vanish by the height of $10D$ above the source. The velocity fluctuations reach a peak value at $4D$ above the source, and the higher the B_o, the higher their magnitude. They persist longer, and at a distance of $12D$ above the source, the magnitude is still significant. The near-source TKE is mainly due to buoyancy-generated turbulence, whereas the shear-generated turbulence contributes to TKE in the far-source region.

3.4. *Flow structures, mixing and entrainment*

In this section, we investigate the mixing processes as the plume expands into the atmosphere, entraining the ambience and spreading radially. We first discuss the flow structures. To understand the differences in the vortex structures between the cases, the following analysis is conducted for all the five cases. The evolution of the isosurfaces of instantaneous buoyancy (g') at two different times corresponding to $t = 400$ and 1300 s after release is shown in figure 12 for all the five cases. After $t = 200$ s, a central core is formed (this is not shown). The time taken for the central core to form is nearly the same for all the cases. As the plume accelerates vertically with increasing mean velocity at the centreline, the velocity difference between the ambience and the core results in the formation and eventual roll-up of the shear layer into primary vortical structures. These arise mainly due to the Kelvin–Helmholtz shear-driven instability. At $t = 400$ s, a well-defined head is evident characterized by instabilities at the interface for cases 2–5. The head has still not formed for the case 1 (lowest forcing), and it forms at a later time. The higher the B_o, the faster is the formation of the head. This happens around $z = 2D$ for all the cases. As the plume travels beyond $z = 2D$, the plume enters a decelerating regime where the centreline mean velocity starts to decay resulting in growth of instabilities, whereupon it becomes unstable and breaks down into smaller vortices. A characteristic feature for all the cases is the development of a well-defined neck region which is capped by the unstable head as seen from figure 12(*b,d,f,h,j*) at time $t = 1300$ s. The vortical structures that form above the neck and that will be referred to as the head region of the plume, grows in size as the plume expands. The higher the B_o, the instabilities in the head
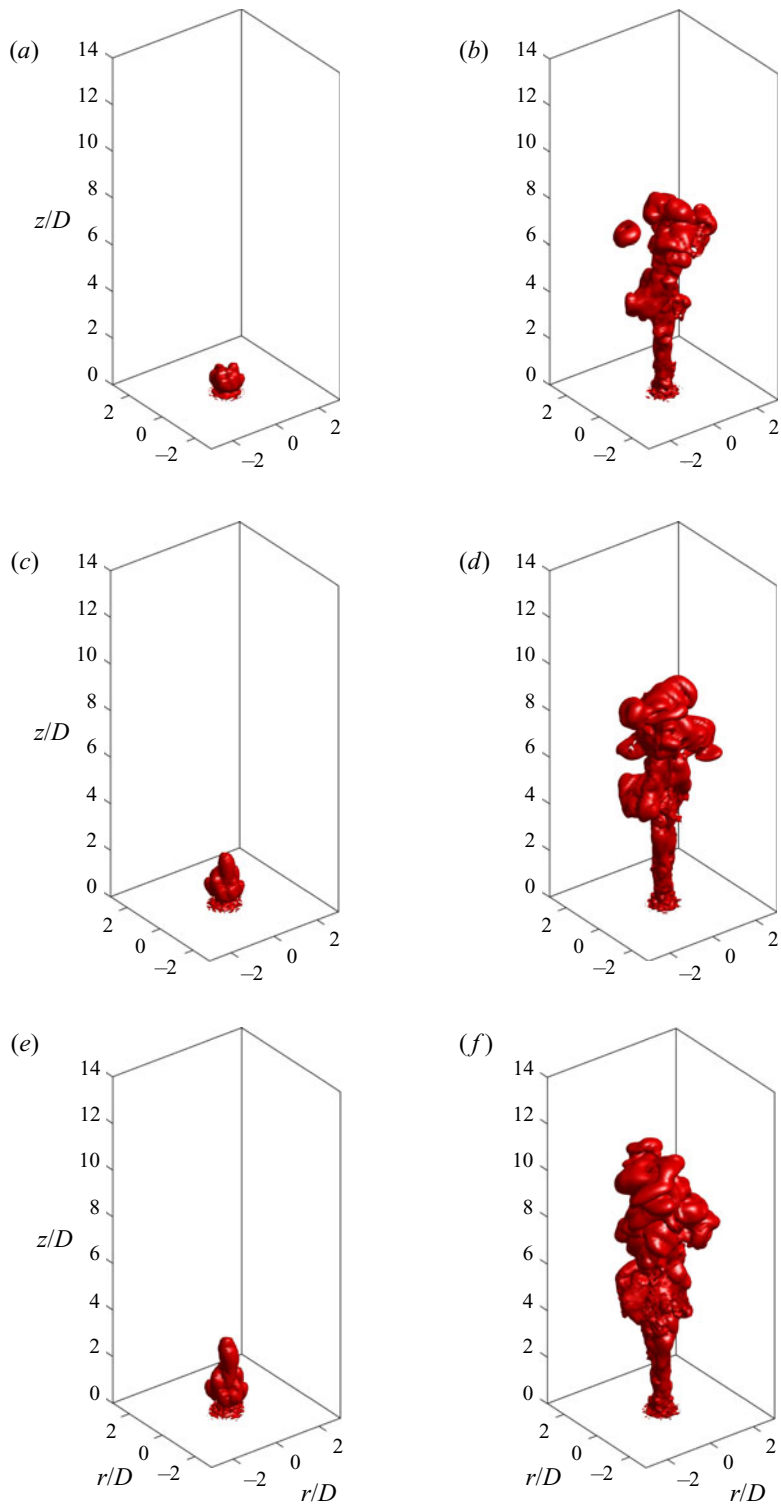
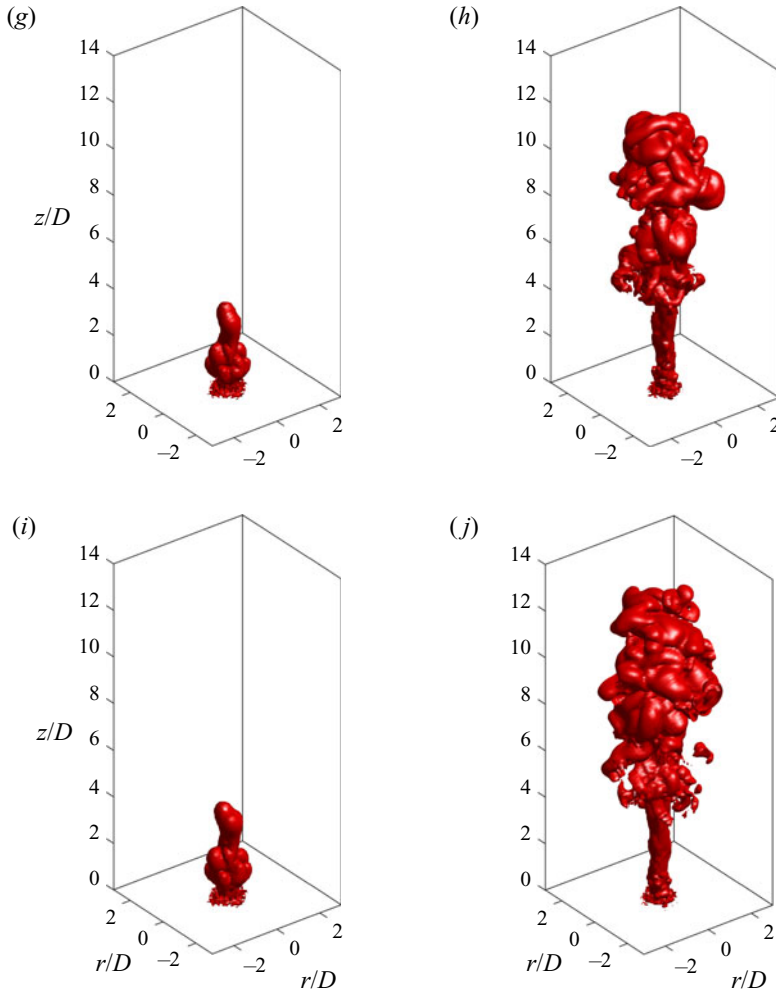FIGURE 12. (*a,b,c,d,e,f*). For caption see next page.

FIGURE 12 (cntd). (*g,h,i,j*). Isosurfaces of instantaneous buoyancy *g′* for case 1 (*a,b*), case 2 (*c,d*), case 3 (*e,f*), case 4 (*g,h*) and case 5 (*i,j*) at *t* = 400 s (*a,c,e,g,i*) and *t* = 1300 s (*b,d,f,h,j*).

region are more dominant that cause the ambient fluid to be entrained into the plume and resulting in increased mixing.

For the rest of the analysis of the flow structures, we present the analysis for one case and for consistency with the rest of the manuscript, we pick case 2. The buoyant fluid from the source rises vertically in a column with an upward-spiralling motion as depicted in figure 13. Figure 13(*a*) shows the λ_2 vortex detection criterion (Jeong & Hussain 1995) which is used to extract the dominant vortex features plotted at time *t* = 1740 s after the initial source release. The conspicuous feature that is evident is the formation of a column of upward-spiralling vortices that is present to a height of *z* = 5*D* above the source. The primary vorticity is generated mainly due to buoyancy. Above the column vortex, horizontal vortex rings form that propagate upwards as the plume grows. The vorticity transport equations dictate that the buoyancy can only generate vorticity in the radial direction, which is the primary component of vorticity; and the tilting of the horizontal vorticity into the axial direction results in the secondary vorticity, thus forming the axial
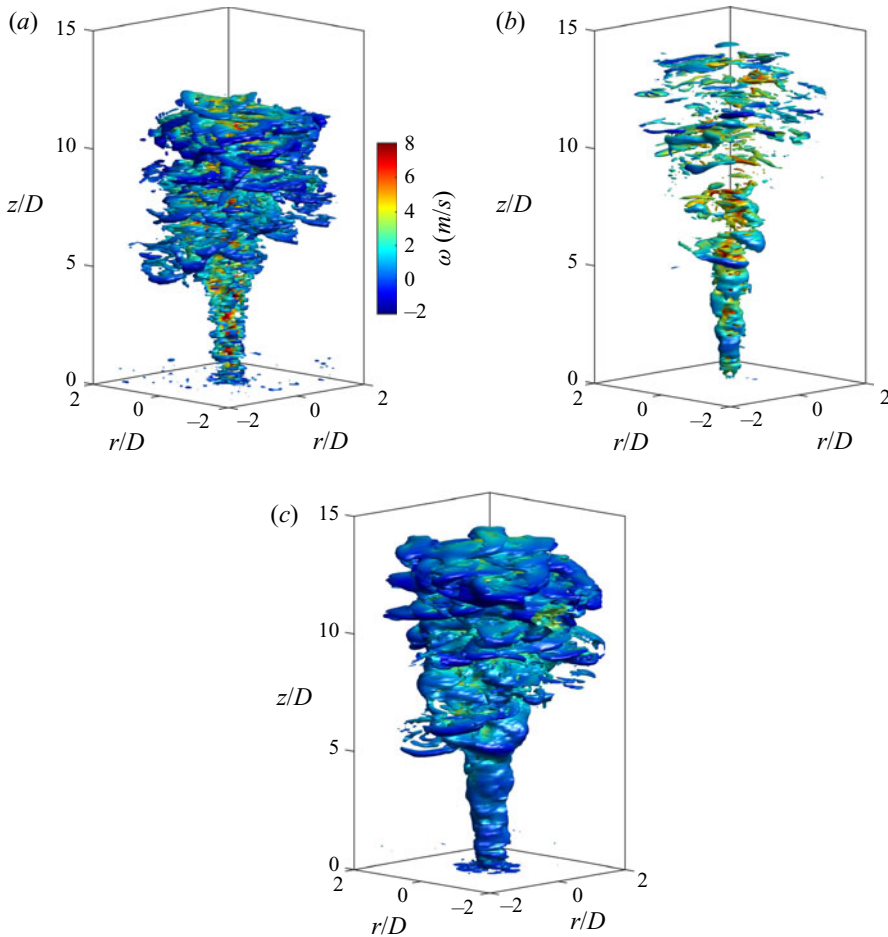
FIGURE 13. For case 2: (*a*) λ_2 vortex detection criterion isosurface with $\lambda_2 = -3e^{-5}$ at $t = 1740$ s, (*b*) 0.05 isosurface of vorticity at $t = 2100$ s, (*c*) 0.02 isosurface of vorticity at $t = 2100$ s. The isosurfaces in (*a–c*) are coloured according to the instantaneous axial velocity, the colourbar is given in (*a*).

vorticity (Tennekes & Lumley 1972). The isosurfaces of vorticity at time $t = 2100$ s are plotted for two different contour values to extract the features of the column vortex and the horizontal vortex rings in figures 13(*b*) and 13(*c*), respectively. The column vortex consists of positive vorticity (clockwise in nature) as it spirals upwards with increasing vorticity. Counter rotating vortices (negative vorticity) stretch in the horizontal plane and expand along the plume direction. Such similar counter-rotating vortices in the far-field aligned with the plume trajectory have been observed for a jet in a cross-flow (Fric & Roshko 1994). Wildland fires have exhibited characteristic horizontal vortex rings, forms that propagate upwards as the plume grows (Forthofer & Goodrick 2011). Figure 14 shows the contours of the instantaneous buoyancy (g') as the plume evolves in time for case 2. At a time $t = 300$ s after the release of the plume, a well-defined head emerges consisting of the heated fluid at source conditions. At $t = 360$ s, instabilities appear near the front and mixing is initiated. At $t = 600$ s, the frontal region of the plume expands with the head still maintaining its shape. At this time, instabilities are initiated at the centreline. As the
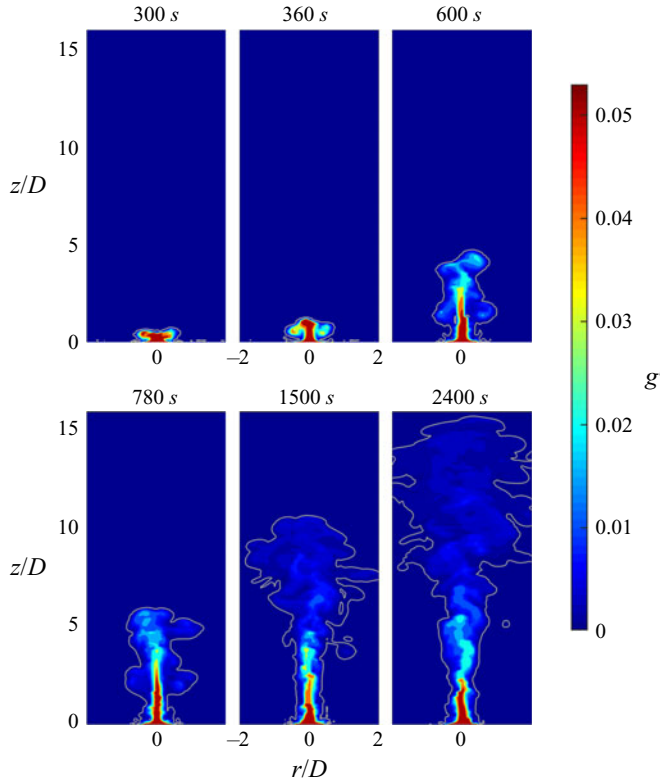
FIGURE 14. Time evolution of instantaneous buoyancy, g', at the centreplane for case 2.

time progresses to $t = 780$, 1500 and 2400 s, the plume expands with increasing dilution near the frontal region of the plume. Even at the later times, the mixing at the central core of the plume starts only beyond a distance of $z = 2D$ from the source. The mixing and entrainment is a highly unsteady process. We will quantify the mixing using a first principles approach.

Figure 15(*a,b*) shows the contour plot of instantaneous radial vorticity and axial vorticity, respectively, as the plume evolves from the source. This is presented for case 2. In the initial stages at $t = 300$, 360 s with the formation of the head, buoyancy generated radial vorticity originates at the source and expands vertically as the plume moves forward. This is seen from figure 15(*a*), which depicts the radial vorticity contours. At later times, the vortex structures around the centreline expand to $z = 5D$ at $t = 780$ s, and beyond which, at later times, i.e. $t = 1500$, 2400 s, the spatial instabilities break the vorticity resulting in the formation of small-scale structures above this height at later times. On the other hand, the axial vorticity that develops is the secondary vorticity from the vortex stretching and tilting processes. It is characterized by small-scale structures even at earlier times. At later times, due to instabilities at the front interface, the vortex breakdown results in the entire plume being dominated by small-scale structures. The unsteady mixing and dilution at the frontal region of the plume results in instabilities and leads to the breakdown of the vorticity to small-scale structures.

Figure 16 shows the instantaneous velocity vectors in the $r–z$ plane at $t = 1300$ s for case 2. Dominant features of the plume include a neck region with a primarily axial component of velocity, and strong instabilities at the plume interface that entrain the
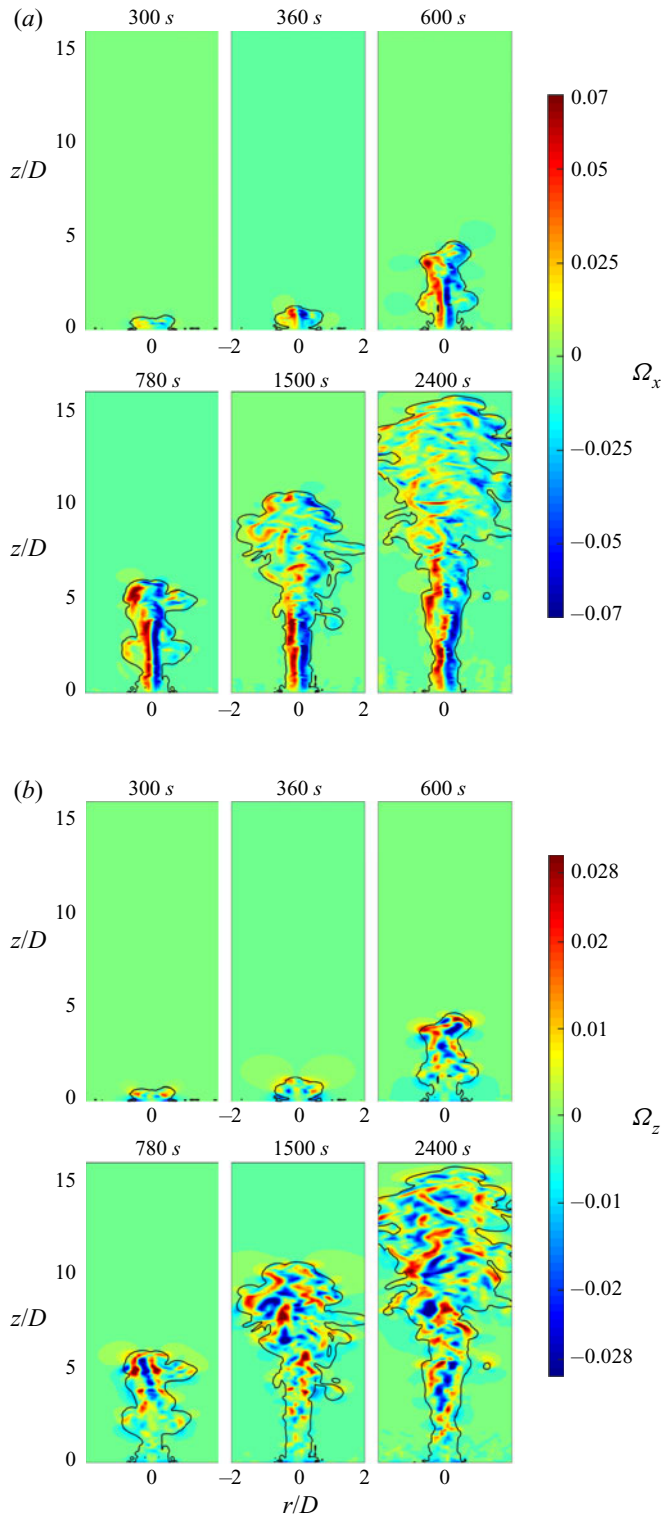
FIGURE 15. Instantaneous snapshots of (*a*) radial vorticity and (*b*) axial vorticity for case 2.
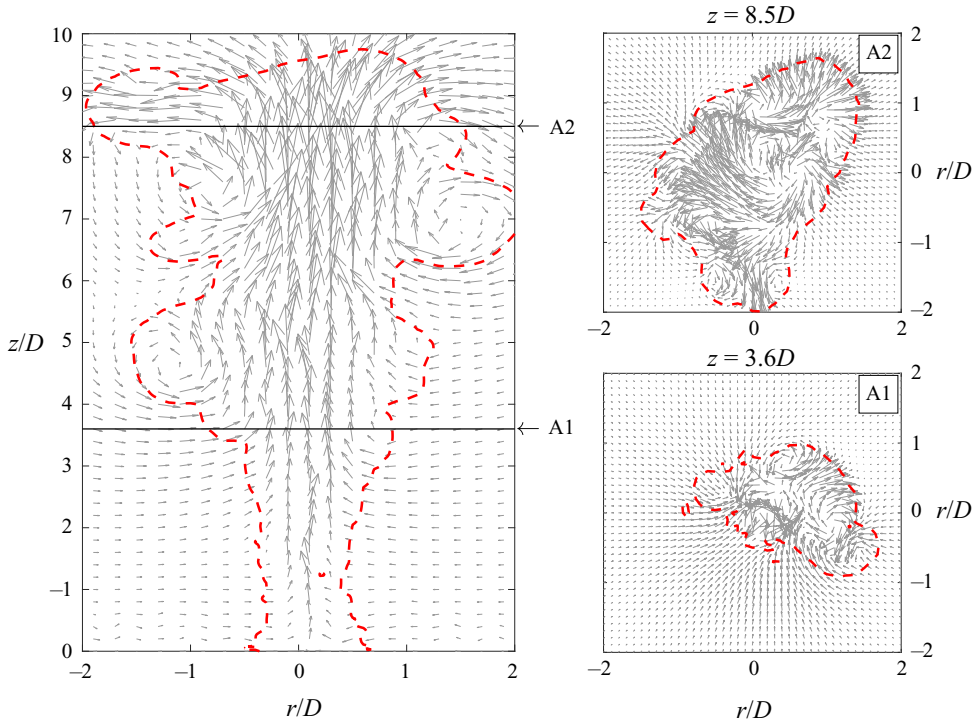
FIGURE 16. For case 2, cross-stream averaged velocity vectors and plume contour selected by g' threshold at centreplane at $t = 1300$ s. Here, A1 and A2 are plume cross-sections at $3.6D$ and $8.5D$, respectively.

ambient fluid into the plume and result in significant mixing. Strong mixing is evident at the frontal region of the plume.

The unsteady entrainment is the most prominent feature of starting buoyant plumes, and it is calculated using first principles as follows: the amount of fluid that entrains into the plume in a small time interval is the change in the volume of the plume during that time period. With increasing source buoyancy flux, the plume expands much faster as the cold ambient entrains more efficiently, mixing and diluting the plume. The instantaneous scaled entrainment E, is the amount of the ambient fluid that enters the current, and it is calculated as the increase of the volume of fluid in the plume due to the radial expansion of the plume with respect to the previous state in time per unit volume of the initial fluid; it is defined as

$$E(t) = \frac{V(t_2) - V(t_1)}{A_{neck} u_f \, dt}. \tag{3.3}$$

Here, $V(t_2)$ and $V(t_1)$ represent the volume of the fluid in the plume at instants $t = t_1$ and t_2, respectively. The radial expansion of the plume during the time interval $dt = t_2 - t_1$ is given as the change of the volume (change of the area times the distance travelled by the plume during this time), where the distance travelled by the plume is $u_f \, dt$ and the area of the initial release is A_{neck}. A similar approach of using the volume-based measure to quantify the entrainment has been conducted successfully by Bhaganagar & Pillalamarri (2017).
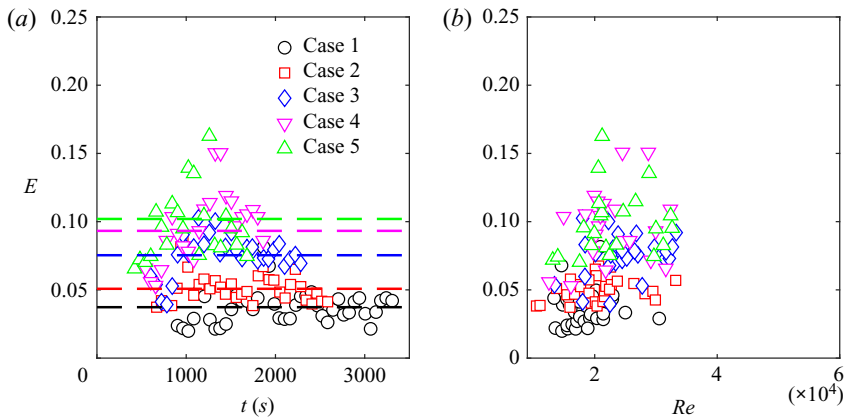
FIGURE 17. (*a*) Variation of the scaled entrainment (*E*). The dashed lines represent the respective average scaled entrainment values over the period plotted. (*b*) Correlation of *E* with local Reynolds number.

Figure 17(*a*) shows the instantaneous scaled entrainment *E* versus time for all the cases. The entrainment begins after the formation of the head (which occurs around $z = 2D$ from the source). It increases to a maximum value and it steadily drops and reaches an asymptotic value, which varies from 0.05–0.08 for cases 1–5. The maximum E is 0.15 for the case with the highest B_o. The time where the peak entrainment occurs correlates with the time when the mixing is initiated in the plume, and due to the entrainment of the cooler ambient fluid into the plume, it undergoes dilution with drastic reduction of the buoyancy. The higher the source buoyancy flux, the higher the entrainment and the longer it takes to reach a steady-state value. Figure 17(*b*) shows the entrainment parameter verses the local Reynolds number. There is a correlation ($R^2 = 0.62 - 0.69$) with the local Reynolds number. This is reasonable as the entrainment occurs in the unstable head region which moves with the front velocity and the local width of the plume. The local Reynolds number has been calculated based on the width of the plume in the head region and the front velocity.

Significant variability in the entrainment coefficient has been reported in the literature. The classical plume theory estimates the entrainment coefficient as 0.15, whereas George *et al.* (1977) estimated the entrainment coefficient in the far-field of the plume as 0.108 in the region where the mean velocity profiles were Gaussian. For Gaussian profiles, the entrainment coefficient has been reported in the range of 0.07–0.11 for pure buoyancy-dominated plumes (Carazzo, Kaminski & Tait 2006). Papanicolau & List (1988) calculated the entrainment coefficient to be 0.0875 for pure plumes.

4. Conclusions

Geophysical turbulent buoyant plumes that occur in the atmosphere have high Reynolds numbers, they expand vertically (several kilometres) and spread radially while entraining the ambient fluid, resulting in substantial mixing. Our understanding of the flow dynamics of starting turbulent buoyant plumes is still very limited. There is no consensus on the centreline mean velocity and buoyancy profiles nor the turbulence measurements such as ratio of the turbulence to the mean flow. Characteristic features of starting plumes from an area release have been reported in various studies as consisting of a converging–diverging region (neck), which is capped by a well-defined head region; however, the flow dynamics

in these regions has not been well understood. Significant knowledge gaps exist in our understanding of the flow physics in the near-source region (0–$15D$) of the plume. To address these issues, a fundamental study has been conducted to understand the mean and turbulence characteristics and the unsteady dynamics of large-scale structures, and their role in mixing processes of starting turbulent plumes initiated from a heated area-release source into the neutral atmosphere. Large eddy simulation has been conducted in a domain of size 7 km in vertical and 4 km × 4 km in horizon. Simulations have been performed for five different cases with source g' of 0.082, 0.145, 0.185, 0.237, 0.272, respectively. The source heat flux is maintained at a constant value ranging from 0.5–2.5 km s^{-1}. We define the plume Reynolds number based on maximum centreline velocity and the plume half-width at this height. With increasing B_o, the plume Reynolds number Re increases from 6×10^7–10^8; however, Fr does not increase monotonically with increasing B_o, and it varies from 1.091–1.149 for the five cases.

Buoyancy plumes released from an area source are characterized by a neck region resembling a column which extends to a height of $5D$ and this region has a characteristic converging–diverging trend where the plume width decreases from the source radius and reaches a minimum, and beyond which the plume expands. The region above this columnar neck is the dynamically active head region where there is an active mixing, entrainment and dilution of the plume. The average value of the plume width of the temperature profile compared with that of the velocity profile above the neck region of the plume has been obtained as 1.15, which is consistent with plume-like behaviours as reported by previous experiments where the buoyancy profiles are wider than the velocity profiles at a given height.

The mean flow developed from the buoyancy forcings accelerates from rest to a maximum value and it starts to decay in height at a rate of a $-1/3$ power law. The maximum velocity occurs in the neck region (varying in the range of $z = 1.62D$–$1.75D$ for the five cases). During the accelerating period, the mean buoyancy is nearly a constant and as the flow starts to decelerates, it also starts to decay, but at a rate of $-5/3$. The radial profiles of the mean temperature and buoyancy reaches a self-similarity behaviour with a Gaussian distribution from a height of $z = 2D$ for all the cases. The mean flow is not self-similar in the neck region. The front velocity and the maximum centreline velocity scales with B_o and z, and can be expressed as $w_f = \xi_f B_o^{1/3} z_f^{-1/3}$ as $w_c = \xi_{wc} B_o^{1/3} z_f^{-1/3}$, respectively. For all the cases, we obtained that the front moves with a non-dimensional velocity (ξ_f) of ~ 2.0 and the non-dimensional maximum centrelinevelocity (ξ_{wc}) is ~ 3.0. The consequence of this is that as the plume advances the fluid from the neck region overrides the front velocity and thus feeds into the head region of the front. It has important implications, resulting in the unsteady mixing and entrainment.

Initially, turbulence is mainly generated from the buoyancy production mechanisms (P_b). The higher the B_o, the higher the initial production of TKE. In the near-source region, $2D$–$4D$, both P_s and P_b contribute to TKE, and with peak production at a radial location of $r = 0.2D$. As the plume grows axially, the location of peak TKE production shifts radially outwards. Due to the radial transport of TKE towards the centreline, the maximum TKE is concentrated at $r/D = 0$. Overall, P_b is higher than P_s. The r.m.s of axial velocity and radial velocity fluctuations build from zero near the wall to quasi-equilibrium value at nearly $5D$, with values ranging from w_{rms} of 0.31–0.35, u_{rms} of 0.21–0.24 and θ_{rms} of 0.48–0.53, respectively. Buoyancy fluctuations are much dominant compared with the velocity fluctuations. It is interesting to note that the neck region of the plume plays an important role in the production of TKE, whereas the peak turbulence is mainly concentrated in the head region of the plume, which is dynamically active.

The entrainment and mixing is a highly unsteady process. Key physical structures that have been observed are the upward spiralling vortex with clockwise vorticity that forms the central core of the plume, and vortex rings that stretch in the horizontal plane which expand along the plume direction. During the initial accelerating stage, a well-defined head is formed that is characterized by a spiralling vortex with ring formation with the dominant radial component of vorticity generated by buoyancy. The primary mechanism for the formation of the head is shear-driven instability. As the plume expands over time, the spiralling central core strengthens that leads the instabilities to break down the structures to small scales in the head region of the plume. The spiralling central core expands to around $5D$, thus forming a neck region and which is capped by the unstable head. This region is characterized by maximum TKE that occurs at the centreline. The fluid in the neck region (maximum centreline velocity occurs between $1.5D$–$1.7D$ for all the cases), travels faster than the front, thus constantly feeding into the head. Unsteady entrainment (E) has been quantified using first principles, and this revealed that, initially the entrainment is negligible until the formation of secondary instabilities leading to the breakdown of the structures. Here, E correlated with the local Reynolds number based on the width of the head (dynamic portion of the plume) and front velocity.

Ultimately, this study is offered as a contribution to improve the understanding of starting plumes released from area source, where there is a scarcity of both experimental and numerical data. A framework has been developed to characterize starting plumes released in atmospheric conditions. The study has direct relevance to important applications for natural disasters, such as wildland-based fires, where the improved understanding of flow characteristics and unsteady entrainment are important for predicting the mixed state of the plume. The present study assumes the ambient air is in a neutral stability state, and future studies will be able to extend the knowledge gained from this study to isolate the effects of atmospheric stability on plume fluid dynamics. The presence of a spiralling column vortex around the central core and the vortex rings that cause the plume to spread as it entrains the surrounding cooler air and mixing rigorously are characteristic features of geophysical plumes. In future, the present study will be extended to include the effect of atmospheric stability on the unsteady entrainment processes, and the modification of the vorticity generation processes and vortex structures will provide key insights to the contribution of the atmospheric convective rolls on modifying the mixing processes.

Declaration of interests

The authors report no conflict of interest.

REFERENCES

ARAKAWA, A. & LAMB, V. R. 1977 Computational design of the basic dynamical processes of the UCLA general circulation model. In *General Circulation Models of the Atmosphere* (ed. J. Chang), Methods in Computational Physics: Advances in Research and Applications, vol. 17, pp. 173–265. Elsevier.

BAINES, P. G. 2001 Mixing in flows down gentle slopes into stratified environments. *J. Fluid Mech.* **443**, 237–270.

BATCHELOR, G. K. 1954 Heat convection and buoyancy effects in fluids. *Q. J. R. Meteorolog. Soc.* **80** (345), 339–358.

BATCHELOR, G. K. 2000 *An Introduction to Fluid Dynamics*. Cambridge University Press.

BHAGANAGAR, K. 2017 Role of head of turbulent 3-d density currents in mixing during slumping regime. *Phys. Fluids* **29** (2), 020703.

BHAGANAGAR, K. & BHIMIREDDY, S. R. 2017 Assessment of the plume dispersion due to chemical attack on April 4, 2017, in Syria. *Nat. Hazards* **88** (3), 1893–1901.

BHAGANAGAR, K. & PILLALAMARRI, N. R. 2017 Lock-exchange release density currents over three-dimensional regular roughness elements. *J. Fluid Mech.* **832**, 793–824.

BHAMIDIPATI, N. & WOODS, A. W. 2017 On the dynamics of starting plumes. *J. Fluid Mech.* **833**.

BRIGGS, G. A. 1972 Chimney plumes in neutral and stable surroundings. *Atmos. Environ.* **6** (7), 507–510.

BUCKINGHAM, S., KOLOSZAR, L., BARTOSIEWICZ, Y. & WINCKELMANS, G. 2017 Optimized temperature perturbation method to generate turbulent inflow conditions for LES/DNS simulations. *Comput. Fluids* **154**, 44–59.

CARAZZO, G., KAMINSKI, E. & TAIT, S. 2006 The route to self-similarity in turbulent jets and plumes. *J. Fluid Mech.* **547**, 137–148.

CARAZZO, G., KAMINSKI, E. & TAIT, S. 2008 On the rise of turbulent plumes: quantitative effects of variable entrainment for submarine hydrothermal vents, terrestrial and extra terrestrial explosive volcanism. *J. Geophys. Res. Solid Earth* **113**, 94–103.

DEARDORFF, J. W. 1980 Stratocumulus-capped mixed layers derived from a three-dimensional model. *Boundary-Layer Meteorol.* **18** (4), 495–527.

DEVENISH, B. J., ROONEY, G. G. & THOMSON, D. J. 2010 Large-eddy simulation of a buoyant plume in uniform and stably stratified environments. *J. Fluid Mech.* **652**, 75–103.

EPSTEIN, M. & BURELBACH, J. P. 2001 Vertical mixing above a steady circular source of buoyancy. *Int. J. Heat Mass Transfer* **44** (3), 525–536.

ERNST, G. G. J., SPARKS, R. S. J., CAREY, S. N. & BURSIK, M. I. 1996 Sedimentation from turbulent jets and plumes. *J. Geophys. Res. Solid Earth* **101** (B3), 5575–5589.

EZZAMEL, A., SALIZZONI, P. & HUNT, G. R. 2015 Dynamical variability of axisymmetric buoyant plumes. *J. Fluid Mech.* **765**, 576–611.

FANNELØP, T. K., HIRSCHBERG, S. & KÜFFER, J. 1991 Surface current and recirculating cells generated by bubble curtains and jets. *J. Fluid Mech.* **229**, 629–657.

FANNELØP, T. K. & WEBBER, D. M. 2003 On buoyant plumes rising from area sources in a calm environment. *J. Fluid Mech.* **497**, 319–334.

FISCHER, H. B., LIST, J. E., KOH, C. R., IMBERGER, J. & BROOKS, N. H. 2013 *Mixing in Inland and Coastal Waters*. Elsevier.

FORTHOFER, J. M. & GOODRICK, S. L. 2011 Review of vortices in wildland fire. *J. Combust.* **2011**, 984363.

FRIC, T. F. & ROSHKO, A. 1994 Vortical structure in the wake of a transverse jet. *J. Fluid Mech.* **279**, 1–47.

FRIEDL, M. J., HÄRTEL, C. & FANNELOP, T. K. 1999 An experimental study of starting plumes over area sources. *Il Nuovo Cimento* **22** (6), 835–846.

FROMM, M. D. & SERVRANCKX, R. 2003 Transport of forest fire smoke above the tropopause by supercell convection. *Geophys. Res. Lett.* **30** (10), L016820.

GARRATT, J. R. 1994 The atmospheric boundary layer. *Earth-Sci. Rev.* **37** (1–2), 89–134.

GEORGE, W. K., ALPERT, R. L. & TAMANINI, F. 1977 Turbulence measurements in an axisymmetric buoyant plume. *Int. J. Heat Mass Transfer* **20** (11), 1145–1154.

HOLT, T. & RAMAN, S. 1988 A review and comparative evaluation of multilevel boundary layer parameterizations for first-order and turbulent kinetic energy closure schemes. *Rev. Geophys.* **26** (4), 761–780.

HUNT, G. R. & KAYE, N. G. 2001 Virtual origin correction for lazy turbulent plumes. *J. Fluid Mech.* **435**, 377–396.

HUNT, G. R. & KAYE, N. B. 2005 Lazy plumes. *J. Fluid Mech.* **533**, 329–338.

JEONG, J. & HUSSAIN, F. 1995 On the identification of a vortex. *J. Fluid Mech.* **285**, 69–94.

KAHN, R. A., CHEN, Y., NELSON, D. L., LEUNG, F., LI, Q., DINER, D. J. & LOGAN, J. A. 2008 Wildfire smoke injection heights: two perspectives from space. *Geophys. Res. Lett.* **35** (4), L04809.

KAMINSKI, E., TAIT, S. & CARAZZO, G. 2005 Turbulent entrainment in jets with arbitrary buoyancy. *J. Fluid Mech.* **526**, 361–376.

KAYE, N. B. & HUNT, G. R. 2009 An experimental study of large area source turbulent plumes. *Int. J. Heat Fluid Flow* **30** (6), 1099–1105.

KOTSOVINOS, N. E. & LIST, E. J. 1977 Plane turbulent buoyant jets. Part 1. Integral properties. *J. Fluid Mech.* **81** (1), 25–44.

LAPRISE, R. 1992 The Euler equations of motion with hydrostatic pressure as an independent variable. *Mon. Weath. Rev.* **120** (1), 197–207.

LINDEN, P. F., BATCHELOR, G. K., MOFFATT, H. K. & WORSTER, M. G. 2000 Convection in the environment. In *Perspectives in Fluid Dynamics: A Collective Introduction to Current Research* (ed. G. K. Batchelor, H. K. Moffatt & M. G. Worster), pp. 289–345. Cambridge University Press.

MARJANOVIC, G., TAUB, G. N. & BALACHANDAR, S. 2019 On the effects of buoyancy on higher order moments in lazy plumes. *J. Turbul.* **20** (2), 121–146.

MOENG, C. H. 1984 A large-eddy-simulation model for the study of planetary boundary-layer turbulence. *J. Atmos. Sci.* **41** (13), 2052–2062.

MORTON, B. R. 1957 Buoyant plumes in a moist atmosphere. *J. Fluid Mech.* **2** (2), 127–144.

MORTON, B. R. 1959 Forced plumes. *J. Fluid Mech.* **5** (1), 151–163.

MORTON, B. R., TAYLOR, G. I. & TURNER, J. S. 1956 Turbulent gravitational convection from maintained and instantaneous sources. *Proc. R. Soc. Lond.* A **234** (1196), 1–23.

O'HERN, T. J., WECKMAN, E. J., GERHART, A. L., TIESZEN, S. R. & SCHEFER, R. W. 2005 Experimental study of a turbulent buoyant helium plume. *J. Fluid Mech.* **544**, 143–171.

ÖZGÖKMEN, T. M., JOHNS, W. E., PETERS, H. & MATT, S. 2003 Turbulent mixing in the red sea outflow plume from a high-resolution nonhydrostatic model. *J. Phys. Oceanogr.* **33** (8), 1846–1869.

PANCHAPAKESAN, N. R. & LUMLEY, J. L. 1993 Turbulence measurements in axisymmetric jets of air and helium. Part 2. Helium jet. *J. Fluid Mech.* **246**, 225–247.

PAPANICOLAU, P. N. & LIST, E. J. 1988 Investigations of round vertical turbulent buoyant jets. *J. Fluid Mech.* **195** (341–391), 168.

PHAM, M. V., PLOURDE, F. & DOAN, K. S. 2005 Three-dimensional characterization of a pure thermal plume. *Trans. ASME: J. Heat Transfer* **127** (6), 624–636.

PHAM, M. V., PLOURDE, F. & DOAN, K. S. 2007 Direct and large-eddy simulations of a pure thermal plume. *Phys. Fluids* **19** (12), 125103.

PLOURDE, F., PHAM, M. V., DOAN, K. S. & BALACHANDAR, S. 2008 Direct numerical simulations of a rapidly expanding thermal plume: structure and entrainment interaction. *J. Fluid Mech.* **604**, 99–123.

RAMAPRIAN, B. R. & CHANDRASEKHARA, M. S. 1989 Measurements in vertical plane turbulent plumes. *Trans. ASME: J. Fluids Engng* **111** (1), 69–77.

SCHLÜTER, J. U., PITSCH, H. & MOIN, P. 2004 Large-eddy simulation inflow conditions for coupling with Reynolds-averaged flow solvers. *AIAA J.* **42** (3), 478–484.

SCHULTZ, A., DELANEY, J. R. & MCDUFF, R. E. 1992 On the partitioning of heat flux between diffuse and point source seafloor venting. *J. Geophys. Res. Solid Earth* **97** (B9), 12299–12314.

SHABBIR, A. & GEORGE, W. K. 1994 Experiments on a round turbulent buoyant plume. *J. Fluid Mech.* **275**, 1–32.

SKAMAROCK, W. C., KLEMP, J. B., DUDHIA, J., GILL, D. O., BARKER, D. M., WANG, W. & POWERS, J. G. 2008 A description of the advanced research WRF version 3. *NCAR Technical Note*-475+ STR. National Center for Atmospheric Research.

SKYLLINGSTAD, E. D. & DENBO, D. W. 2001 Turbulence beneath sea ice and leads: a coupled sea ice/large-eddy simulation study. *J. Geophys. Res. Oceans* **106** (C2), 2477–2497.

TAUB, G. N., LEE, H., BALACHANDAR, S. & SHERIF, S. A. 2015 An examination of the high-order statistics of developing jets, lazy and forced plumes at various axial distances from their source. *J. Turbul.* **16** (10), 950–978.

TENNEKES, H. & LUMLEY, J. L. 1972 *A First Course in Turbulence*. MIT.

TURNER, J. S. 1962 The 'starting plume' in neutral surroundings. *J. Fluid Mech.* **13** (3), 356–368.

TURNER, J. S. 1969 Buoyant plumes and thermals. *Annu. Rev. Fluid Mech.* **1** (1), 29–44.

VAN REEUWIJK, M, SALIZZONI, P., HUNT, G. R. & CRASKE, J. 2016 Turbulent transport and entrainment in jets and plumes: a DNS study. *Phys. Rev. Fluids* **1** (7), 074301.

WANG, H. & LAW, A. W. 2002 Second-order integral model for a round turbulent buoyant jet. *J. Fluid Mech.* **459**, 397–428.

WICKER, L. J. & SKAMAROCK, W. C. 2002 Time-splitting methods for elastic models using forward time schemes. *Mon. Weath. Rev.* **130** (8), 2088–2097.

WIDELL, K., FER, I. & HAUGAN, P. M. 2006 Salt release from warming sea ice. *Geophys. Res. Lett.* **33** (12), L12501.

WOODS, A. W. 2010 Turbulent plumes in nature. *Annu. Rev. Fluid Mech.* **42**, 391–412.

WU, XIAOHUA 2017 Inflow turbulence generation methods. *Annu. Rev. Fluid Mech.* **49**, 23–49.

YANG, C. & CAI, X. 2014 A scalable fully implicit compressible Euler solver for mesoscale nonhydrostatic simulation of atmospheric flows. *SIAM J. Sci. Comput.* **36** (5), S23–S47.